Nature of High- and Low-Affinity Metal Surface Sites on Birnessite Nanosheets

Alain Manceau, Stephan Steinmann

Alain Manceau, Stephan Steinmann. Nature of High- and Low-Affinity Metal Surface Sites on Birnessite Nanosheets. ACS Earth and Space Chemistry, 2021, 5 (1), pp.66-76. 10.1021/acsearthspacechem.0c00278 . hal-03144115

The Nature of High and Low Affinity Metal Surface Sites on Birnessite Nanosheets

Alain Manceau*[a] and Stephan N. Steinmann[b]

[a] Univ. Grenoble Alpes, CNRS, ISTerre, CS 40700, 38058 Grenoble, France
[b] Univ. Lyon, ENS de Lyon, CNRS, Laboratoire de Chimie, 69342 Lyon, France

Corresponding Author :
alain.manceau@univ-grenoble-alpes.fr

Keywords: Phyllomanganate, DFT, EXAFS, adsorption, nickel, copper, zinc, lead

ABSTRACT

Birnessite nanosheets (δ-MnO_2) are key reactive nanoparticles that regulate metal cycling in terrestrial and marine settings, yet there is no molecular explanation for the sorption selectivity of metals which controls their enrichment. This fundamental question was addressed by optimizing the structure of the Ni, Cu, Zn, and Pb surface complexes on δ-MnO_2 and by calculating the Gibbs free energy change (ΔG) of the sorption reactions with density functional theory. The sorption selectivity follows the order Pb > Cu > Ni > Zn, in good agreement with experimental data. Cu, Ni, and Zn bind preferentially to layer edges at low surface coverage forming double-edge-sharing (DES) complexes, whereas Pb binds extensively with high selectivity over the three transition metals to both layer edges (DES bonding) and to basal planes forming triple-corner-sharing (TCS) complexes. Pb has similar affinity for the DES and TCS sites at pH 5 and a higher affinity for the TCS sites at circumneutral pH. The Pb DES and TCS complexes are both dehydrated at the δ-MnO_2-water interface and feature a trigonal pyramidal geometry with three surface O atoms. The high stability of the two new complexes arises from the hybridization between the Pb 6s/6p and the O 2p states, forming a strongly covalent Pb-O/OH bond at the δ-MnO_2 surface. The quantum chemical results provide mechanistic and energetics insight on metal uptake on δ-MnO_2 that extends what extended X-ray absorption fine structure (EXAFS) spectroscopy alone can provide.

INTRODUCTION

Since its discovery in 1956 at Birness, Scotland,[1] the layered manganese oxide birnessite has been recognized as the most abundant manganese oxide in the Earth surface environment and a key reactive mineral that regulates the geochemical cycling of trace metals.[2, 3] Metal-containing birnessite (MeBi) has been documented in soils, mineral and rock coatings, sediments, and marine ferromanganese crusts and nodules.[4-31] Birnessite also features promising electrochemical energy storage performance and catalytic capabilities when fabricated under appropriate conditions,[32-36] and its high sorption capacity can be used in waste water treatment.[37-39] Birnessite is a phyllomanganate, meaning a layered compound composed of edge-sharing $Mn(IV)O_6$ octahedra, with ideal chemical formula MnO_2. However, birnessite is never stoichiometric. The formula of the 1956's specimen was $Na_{0.7}Ca_{0.3}Mn_7O_{14}\cdot 2.8H_2O$, implying that the MnO_2 layer had a permanent negative charge balanced by interlayer Na(I) and Ca(II) cations. There has been a consensus early on to attribute the net layer charge to Mn(III) for Mn(IV) substitution and/or to vacant octahedral site,[40, 41] but its exact nature had remained enigmatic until the successful electron diffraction analysis by Drits et al.,[42] and the Mn-EXAFS spectroscopy study and detailed chemical analysis by Silvester et al.[43] in 1997.

Two species of birnessite are known, a monoclinic/triclinic one of ideal formula $Na^{+}_{0.333}(Mn^{4+}_{0.667}Mn^{3+}_{0.333})O_2$,[42, 44] and an hexagonal one of generic formula $H^{+}_{x}Mn^{3+}_{y}Mn^{2+}_{z}(Mn^{4+}_{u}Mn^{3+}_{v}\square_{w})O_2$,[45] in which □ denotes an empty Mn(IV) position. Hexagonal birnessite (HBi) is the ubiquitous form in nature, and the one formed by bacteria and fungi.[46-54] Structural data indicate that the main metal sorption site is located on the three doubly-coordinated oxygens (O_{2Mn}) positioned above and below each Mn(IV) vacancy (Figure 1a). At pH 5-7 and in the absence of solute ion, each set of three O_{2Mn} shares two protons (+2 charge). Thus, the six O_{2Mn} on the two layer sides of a vacancy carry altogether a total protonic charge of +4, which balances the -4 charge deficit created by the empty Mn(IV) position.

Using Zn-EXAFS, Silvester et al.[43] also found in 1997 that the two protons on one side of a vacancy can be displaced by a Zn(II) ion at pH 4 to form an interlayer triple-corner-sharing (TCS) inner-sphere surface complex on basal planes (Figure 1b). The same year, Manceau et al.[55] described the incorporation at pH 4 of Co(III) into the octahedral vacancy (incorporated INC complex), consecutively to the oxidation of a Co(II) TCS complex by a layer Mn(III) cation which was reduced to $Mn(II)_{(aq)}$. These early studies were performed on well-crystallized HBi having micrometer sized basal planes and 0.16 vacancy per Mn atom.[56] However, natural birnessite is usually nanoparticulate (form denominated δ-MnO_2[57, 58]), and it was recognized in the 2000s that external surfaces, including external vacancies and layer edges, dominate the total reactive surface area as the density of edge sites increases when the lateral layer dimension decreases. In contrast, the density of vacancies is independent of the layer dimension. On a layer edge, a metal can form a double-corner-sharing (DCS) complex, and a double- (DES) or a single-edge-sharing (SES) complex (Figure 1c-e). A DES complex can evolve into a triple-edge-sharing complex (TES) and incorporated progressively into the MnO_2 layer during the crystal growth. The identification of some of the surface species (INC, TCS, DCS, DES) has led to accelerating research aimed to understand their thermodynamic stability,[59-61] and how the mineral structure, layer size, and chemical composition control the metal sorption selectivity and capacity per specific surface area.[24, 37, 62-84]

The most compelling work on the relative affinity of a metal for the vacancy and edge sites has been performed by Takahashi et al.[8] in 2007 with Pb sorbed at pH 5 using EXAFS. This work was able to discern the Pb DES complex on layer edges and the Pb TCS complex on vacancies at a Pb/Mn at. ratio of 0.002, 0.044, 0.112, and 0.197 on δ-MnO_2 and at a ratio of 0.031 on well-crystallized birnessite. The equilibrium structure of Pb(II) shifted from a dominant DES coordination to a dominant TCS coordination at increasing surface coverage on δ-MnO_2, whereas only the TCS coordination was detected at low coverage on birnessite. This result reflects a higher affinity (i.e., a higher thermodynamic stability) of Pb(II) for the DES sites on layer edges than for the TCS sites, whether they are located on basal planes or near a layer edge (i.e., external vacancies). Similarly, Qin et al.[85] showed in 2019 that the proportion of edge to corner Sb(V) complexes on δ-MnO_2 increases with a decrease of the Sb/Mn at. ratio from 0.01 to 0.001, and was higher on δ-MnO_2 than on birnessite at Sb/Mn = 0.01. These results corroborate the rationale that lower crystallinity implies a higher density of reactive sites.[56]

In contrast to Pb(II), Ni(II) and Cu(II) are small enough to be incorporated into a vacancy site of a MnO_2 layer like Co(III) (INC complex).[7, 10, 16, 71, 86, 87] The migration of a Me(II) cation from a TCS site to an INC site is pH-dependent. It is favored at circumneutral pH when the three O_{2Mn} situated on the opposite site of the cavity are deprotonated to suppress the otherwise strong Me(II)-$2H^+$ electrostatic repulsion.[61, 88] The TCS-INC chemical reaction has attracted large scientific attention in the last decade.[88-91] Ni is totally incorporated into the octahedral sheets of phyllomanganates in ferromanganese precipitates and nodules from soils and marine environments.[6, 9, 10, 31, 92] The TCS coordination is considered to be the high energy surface site for Ni, and the main mechanism for Ni enrichment up to percent levels by mass in natural layer-type Mn(IV) oxide minerals is thought to follow the TCS-INC pathway. This view conflicts, however, with two observations.

First, the complete incorporation of Ni in an octahedral layer observed naturally has never been reproduced experimentally. The percentages of Ni in INC and TCS coordinations on δ-MnO_2 were 48% and 52% at Ni/Mn = 0.01 pH 6.6,[90], 45% and 65% at Ni/Mn = 0.002 pH 7,[16] 31% and 69% at Ni/Mn = 0.02 pH 7.7-8.0,[91] 30% and 70% at Ni/Mn = 0.06 pH 8.[88] There seems to be a limit of 50% to the partitioning of Ni in the INC site when it is incorporated via a TCS complex. Second, a Ni-Mn edge-sharing coordination was observed on δ-MnO_2 at Ni/Mn = 0.002 pH 4.[16] At this pH the three O_{2Mn} of a vacancy are protonated, therefore the TCS-INC pathway is less likely. Formation of a DES complex should be preferred to that of an INC complex, as the former involves the deprotonation of only one O_{2Mn} (Figure 1d). These observations challenge the TCS-INC pathway for the incorporation of Ni in the layer of natural phyllomanganates, and suggest that it is incorporated instead on the edges of the octahedral layers during the crystal growth (DES-INC pathway). That layer edge sites have higher surface reactivity toward Ni is consistent with the faster rates of oxidation of As(III) to As(V),[56] and of Co(II) to Co(III),[72, 93] on the layer edge sites of δ-MnO_2 and birnessite relative to vacancy sites.

How can the hypothesis of the sorption of Ni on layer edge sites at low surface coverage be reconciled with spectroscopic results? The Ni-INC, Ni-DES, Ni-TCS, and Ni-DCS complexes are differentiated in EXAFS on the basis of (1) the Ni-Mn interatomic distances, equal to ~2.90 Å for an edge linkage (Ni-INC and Ni-DES), and ~3.48 Å for a corner linkage (Ni-TCS and Ni-DCS), and (2) the number of octahedral linkages, which is six for the INC and TCS coordinations and two for the DES and DCS coordinations (Figure 1). However, coordination numbers (*CN*s) are poorly constrained in EXAFS because this fit parameter is correlated with the disorder parameter σ (Å), expressed as the mean-square displacement of bond length. The low precision on *CN* values, compounded by the overlap of the Ni-INC and Ni-DES distances (~2.90 Å) and the Ni-TCS and Ni-DCS distances (~2.48 Å), complicates the analysis of EXAFS spectra and is a source of uncertainty in the characterization and quantification of the surface species.[90] The INC-DES ambiguity is specific to cations that can substitute for Mn(IV) and Mn(III) in the octahedral layer, which is why Pb(II) is a good chemical probe of the relative affinity of metals for the vacancy and layer edge sites.

Another experimental approach to probing the highest energy surface sites is to measure the EXAFS spectra at low Me/surface area ratio, when the adsorbed cation does not form a mixture of surface species at equilibrium. This has been performed for Pb(II) on δ-MnO_2 (Pb/Mn = 0.002) and Cd(II) on goethite (α-FeOOH) and hydrous ferric oxide (HFO, Cd/Fe = 0.001).[8, 94] However, measuring Ni at low surface coverage is difficult, because of the high X-ray fluorescence yield of the MnO_2/FeOOH/HFO matrix at the absorption edge energy of first-raw transition metals above the Mn and Fe K-edges (i.e., Co, Ni, Cu and Zn). The background fluorescence signal severely degrades the signal-to-noise ratio of EXAFS data, preventing to obtain reliable structural parameters.

In this study, the reactivity of layer edge sites versus vacancy sites was assessed by calculating the thermodynamic stability of the TCS, DCS, DES, and SES surface complexes for Ni(II), Cu(II), Zn(II), and Pb(II). The metal binding constants to the surface sites (K_{Me}) were obtained from the Gibbs free energy changes (ΔG) for transferring the metal cation from an aqueous solution to the surface site (TCS, DCS, DES, SES complexation). Zn does not invade vacancy sites like Pb(II), but it forms more regular ZnO_6 octahedra than Pb(II) and it has a large size difference (0.74 Å vs 1.19 Å), which may influence the energetics of the bonding at the layer surface.

METHODS

Complexation models. A MnO_2 nanolayer, denoted Mn_6V, was constructed. It has a vacancy site at the center, a composition $Mn_6O_{24}H_{22}$, and a total charge of -2 (Figure 1a). The deficit of +4 charge resulting from the Mn(IV) vacancy was balanced by protonating two of the three O_{2Mn} bordering the vacancy on each side of the MnO_2 layer.[43, 59] Unsaturated O ions on layer edges were protonated. The magnetic ordering was ferromagnetic among the Mn ions and antiferromagnetic between Ni/Cu and the Mn ions.[61, 71] Inclusion of magnetism did not decrease ΔG for Cu ($\Delta(\Delta G) < 1$ kcal/mol), and marginally for Ni ($\Delta(\Delta G) < 2$ kcal/mol), thus displacing slightly the equilibrium reactions forward.

Ni^{2+} and Zn^{2+} are octahedrally coordinated in solution and at the MnO_2 surface. Aqua Cu^{2+} fluctuates between tetragonally elongated octahedral (Jahn-Teller distortion, JT), square pyramidal (five-fold), and trigonal bipyramidal (five-fold) coordination, with an average number estimated to 5.7 H_2O molecules.[95] Cu^{2+} was considered to be only hexahydrated in solution, and six-fold or five-fold coordinated on the Mn_6V nanolayers. The ΔG values of the six-fold surface complexes were calculated for the following surface reactions,[96, 97] where Me stands for Ni, Cu, and Zn

$$^{VI}\text{TCS: } Mn_6O_{24}H_{22} + Me(H_2O)_6 \rightarrow Me(H_2O)_3\text{-}Mn_6O_{24}H_{20} + 2H^+ + 3H_2O \quad (1)$$

$$^{VI}\text{DCS: } Mn_6O_{24}H_{22} + Me(H_2O)_6 \rightarrow Me(H_2O)_4\text{-}Mn_6O_{24}H_{22} + 2H_2O \quad (2)$$

$$^{VI}\text{DES: } Mn_6O_{24}H_{22} + Me(H_2O)_6 \rightarrow Me(H_2O)_3\text{-}Mn_6O_{24}H_{21} + H^+ + 3H_2O \quad (3)$$

$$^{VI}\text{SES: } Mn_6O_{24}H_{22} + Me(H_2O)_6 \rightarrow Me(H_2O)_4\text{-}Mn_6O_{24}H_{22} + 2H_2O \quad (4)$$

The reactions for the formation of the five-fold Cu complexes are written

$$^{V}\text{TCS: } Mn_6O_{24}H_{22} + Cu(H_2O)_6 \rightarrow Me(H_2O)_2\text{-}Mn_6O_{24}H_{20} + 2H^+ + 4H_2O \quad (5)$$

$$^{V}\text{DCS: } Mn_6O_{24}H_{22} + Cu(H_2O)_6 \rightarrow Me(H_2O)_3\text{-}Mn_6O_{24}H_{22} + 3H_2O \quad (6)$$

^{V}DES: $Mn_6O_{24}H_{22} + Cu(H_2O)_6 \rightarrow Me(H_2O)_2\text{-}Mn_6O_{24}H_{21} + H^+ + 4H_2O$ (7)

^{V}SES: $Mn_6O_{24}H_{22} + Cu(H_2O)_6 \rightarrow Me(H_2O)_3\text{-}Mn_6O_{24}H_{22} + 3H_2O$ (8)

Various estimates place the number of Pb^{2+}-bound water molecules between 4 and 7.5, on the basis of mobility measurements in aqueous solution.[98] The coordination of Pb^{2+} (electronic configuration $[Xe]6s^2 4f^{14} 5d^{10} 6p^2$) is complicated by the presence of a $6s^2$ electron lone pair on the ion. The result is the prevalence of pyramidal over octahedral configurations in crystallographic structures of Pb(II) with the outer lone pair of electrons at the top of the pyramid.[99] The hexahydrated Pb^{2+} ion (denoted ^{VI}Pb) adopts a trigonal pyramidal geometry with three O atoms at 2.48-2.51 Å and a planar trigonal geometry with the three other O atoms at 2.61-2.72 Å (Figure 2a). The average DFT distance of ^{VI}Pb is identical to the EXAFS Pb-O distance measured in water (2.59 Å), suggesting that the ^{VI}Pb coordination structure prevails.[100] The two most stable four-fold configurations optimized in the gas phase are the seesaw $[Pb(H_2O)_4]^{2+}$ geometry[99] and the 3+1 $[Pb(H_2O)_3(H_2O)]^{2+}$ geometry.[101] In the seesaw geometry (denoted ^{IV}Pb), the two short Pb-O distances are ~2.40 Å, and the two long Pb-O distances are ~2.50 Å (Figure 2b). In the 3+1 configuration, three H_2O molecules form a trigonal coordination at 2.37-2.40 Å from Pb^{2+} (denoted ^{III}Pb), and the fourth H_2O molecule is in a secondary solvation shell at ~3.96 Å from Pb^{2+} and is hydrogen bonded to two coordinating H_2O molecules (Figure 2c). Previous DFT calculations showed that the trihydrated 3+1 coordination is more stable by 5.1 kcal/mol than the tetrahydrated coordination in the gas phase.[101] We obtained a difference of 2.40 kcal/mol in solution using the DFT scheme described below, and no difference (-0.2 kcal/mol) using the CCSD(T)/MP2 molecular orbital theory. Sorption of the $[Pb(H_2O)_4]^{2+}$ ion gives a ΔG value 10 kcal/mol higher (i.e., less negative) than that of the $[Pb(H_2O)_6]^{2+}$ ion, because the loss of two Pb-bound water molecules is exergonic. On the basis of EXAFS[100, 102] and DFT Pb-O distances, we assume that $[Pb(H_2O)_6]^{2+}$ is more abundant than $[Pb(H_2O)_4]^{2+}$ in aqueous solution, although the relative energies suggest otherwise. Given that previous theoretical studies have obtained varying results depending on the level of theory,[103] only DFT-based molecular dynamics simulations in explicit solvent using the same level of theory could clarify the actual situation, but such an investigation is beyond the scope of the present study.

We found that the lowest energy surface complexes are completely or partially dehydrated at the MnO_2 surface. Therefore, the generic surface reactions for Pb^{2+} can be written:

$$Mn_6O_{24}H_{22} + Pb(H_2O)_6 \rightarrow Me(H_2O)_{6-x}\text{-}Mn_6O_{24}H_{22-y} + H^+_y + xH_2O;\ 0 \le y \le 2$$

Thermochemical calculations. Equilibrium geometries and energies were calculated with spin-polarized molecular density functional theory (DFT) using the hybrid generalized-gradient approximation (GGA) as implemented in the Perdew Burke and Ernzerhof functional PBE0[104, 105] (also called PBE1PBE) to describe the exchange-correlation functional.[106] This hybrid functional performs extremely well for geometry and energetic properties.[107] The valence electronic configurations of all atoms were treated with the all-electron polarized def2-TZVP basis sets of triple ζ quality.[108] All basis sets were used in combination with the Coulomb fitting auxiliary def2 /J basis sets.[109] The scalar relativity of Pb was accounted for by replacing the 60 innermost electrons with the def2-ECP effective core potential (ECP), as obtained from the Stuttgart pseudopotential library. The atom-pairwise dispersion correction D3BJ[110] was applied to all atoms. The solvation model based on density (SMD)[111] with water as the solvent was applied to all calculations. The default SMD radii for all elements considered here are equivalent to Bondi's values, which are expected to give most reliable results.[112, 113] The proton solvation energy was taken to be −264.0 kcal/mol.[114]

Vibrational frequency calculations were performed on all optimized geometries to obtain enthalpies and Gibbs free energies of complexation. The total entropy of the unreacted and reacted birnessite models was obtained by summing the electronic and vibrational entropy, omitting rotational and translational entropies as atoms are held together in a solid.[115] The hessian matrix was calculated numerically by finite differences based on the analytical energy gradients as implemented in ORCA under the keyword "NumFreq". All energies are reported at a standard state of 1 mol L^{-1} and 298.15 K. All ab initio computations were carried out using the molecular orbitals calculation software ORCA 4.2.1, and the TightSCF geometry convergence criteria which set the energy change between SCF optimization cycles to 10^{-8} Eh.[116] We carefully checked that the minimum of the total energy was a global minimum. The size of the nanosheet is at the limit of what is currently feasible at this level of theory with a reasonable computational effort.

Equilibrium constants were calculated from $\Delta G = -RT \ln K$, and the molar ratios of the complexed ([Me-MnO_2]) to aqueous ($[Me]_{aq}$) metals calculated from the law of mass action at pH 5 and 7. The accuracy of the reaction entropies was assessed with respect to the prediction of the first hydrolysis constants of the hexa-solvated Mn^{2+}, Ni^{2+}, and Zn^{2+} ions.[117] Calculated pK_a values for the $MnOH^+$ (10.6), $Ni(OH)^+$ (9.9), and $Zn(OH)^+$ (9.0) species differ from experimental values by 0.8(4), which corresponds to a variation of 1-2 kcal/mol on ΔG (Table S1). Thus, absolute ΔG of complexation are calculated reliably within chemical accuracy using the def2-TZVP basis sets for the sorbed metal ions (Me^{2+}). The precision on the variation of the predicted equilibrium constants (i.e., ΔK) is about one power of ten (i.e., log $K \pm 1$).

RESULTS AND DISCUSSION

Structure of the surface complexes. All hydrated surface complexes are stabilized on the Mn_6V nanolayers with H-bonds between water molecules and dangling surface OH groups and O_{2Mn} atoms (Figures 1 and S1). The structures of the DCS, DES, and SES complexes are independent of the layer dimension since they are located on lateral sites. The three water molecules of the TCS complex are H-bonded to three external OH_{2Mn} atoms in the Mn_6V model. On the basal plane of a MnO_2 layer, the surface oxygens are bonded to three Mn atoms, therefore the H-bonds of the TCS complex would be with three O_{3Mn} atoms, not with three OH_{2Mn}. We verified with a $Mn_{18}V$ cluster that the geometry of the TCS complex remained unchanged when the three OH_{2Mn} atoms were replaced with three O_{3Mn} atoms (Figure S2). The calculated Me-O and Me-Mn distances are practically identical to previous DFT[59-61, 71, 88, 90] and EXAFS values[4-10, 43, 67-71, 86-89, 118-122] (Table S2). The mean (Ni,Zn)-(O,OH,H_2O) distances are: Ni-O = 2.03-2.14 Å ± 0.00-0.03 and Zn-O = 2.05-2.20 Å ± 0.00-0.10 Å. The bond lengths of Ni and Zn with H_2O are longer than with O and OH, except for the DES complexes. The Cu-O distances are characteristic of the JT distortion, regardless of the surface coordination of Cu: $^{VI}Cu\text{-}O_{eq}$ = 1.98-2.00 Å ± 0.02-0.06 Å; $^{VI}Cu\text{-}O_{ax}$ = 2.33-2.43 Å ± 0.00-0.14 Å; $^{V}Cu\text{-}O_{eq}$ = 1.97-1.99 Å ± 0.01-0.06 Å; and $^{V}Cu\text{-}O_{ax}$ = 2.21-2.32 Å. The largest difference of 0.14 Å between the two $(^{VI}Cu\text{-}O)_{ax}$ axial ligands occurs for Cu-TCS, where the ^{VI}Cu-O distances to the surface and water oxygen are $d(^{VI}Cu\text{-}O_{2Mn})$ = 2.28 Å and $d(^{VI}Cu\text{-}O_{2H})$ = 2.56 Å (Figure S3a). The $^{VI}CuO_6$ polyhedron has a geometry intermediate between a tetragonally elongated octahedron and a square pyramid, in line with previous DFT[61] and EXAFS[118] results. The longer bond distance of 2.56 Å is lost in the ^{V}Cu complex, which has a square pyramid geometry with $d(^{V}Cu\text{-}O_{2Mn})$ = 2.25 Å in excellent agreement with the EXAFS value of 2.23 Å[118] (Figure 1f). The tetrahedral coordination hypothesized by Sherman and coworkers[123-126] is an incompatible model: it yields short *d*(Cu-Mn) of 3.07-3.10 Å not observed by EXAFS,[118, 123] and the free energy of complexation is as high as 248 kcal/mol (Figure S3b).

Pb adopts a seesaw (^{IV}Pb) or trigonal (^{III}Pb) pyramidal geometry at the MnO_2 surface (Figure 3). The octahedral coordination (^{VI}Pb) was either unstable, or metastable with a moderately positive ΔG value. The first case is illustrated in Figure 3a with the ^{IV}Pb-DCS complex $Pb(2O_{Mn}2H_2O)\cdot 2H_2O$-DCS. The complex was initally ^{VI}Pb-DCS ($Pb(2O_{Mn}4H_2O)$ coordination) and it lost two H_2O ligands during optimization taking on the seesaw $Pb(2O_{Mn}2H_2O)$ coordination. Each departed H_2O ligand is H-bonded to a long Pb-H_2O bond from the seesaw complex and to surface OH groups. The second case is illustrated in Figure 3b,c with the ^{VI}Pb-TCS complex ($Pb(3O_{2Mn}3H_2O)$ coordination, Figure 3b). Its geometry was shown previously to be stable,[60] which our geometry minimization confirmed

(Figure 3b). However, ΔG = +1.8 kcal/mol, indicating that the optimized structure is at best metastable. We found another structure 23.3 kcal/mol more stable (ΔG = -17.9 kcal/mol), in which the surface complex is dehydrated (Pb($3O_{2Mn}$) coordination) and the three departed H_2O are 3.15-4.36 Å away from Pb and are H-bonded to surface O/OH (Figure 3c). The Pb-O_{2Mn} distances are 2.28-2.29 Å, 0.10 Å shorter than the Pb-O distances of the 3+1 aqua species (Figure 2c), and 0.02-0.03 Å shorter than the Pb-O distance of tetragonal PbO (litharge, 2.31 Å). This is accomplished by bringing the Pb atom close to the Mn vacancy, 1.3 Å above the O_{2Mn} plane. Similarly to the ambiguous coordination of Pb^{2+} in solution, explicit solvent molecular dynamics simulations would be necessary to ascertain the hydration state of the PbO_x-TCS complex. However, given the large energy difference (> 20 kcal/mol), we discard the ^{VI}Pb-TCS complex, Pb($3O_{2Mn}3H_2O$), for the energetic discussion below.

The weaker stability of the Pb bond to H_2O compared to surface O atoms and OH groups is reflected electronically in a difference of hybridization between the Pb 6s/6p and the O 2 p states. Calculation of the partial density of states (PDOS) shows that the Pb 6s states are split into one maximum located at the top and another located at the bottom of the valence band (Figure 4). The high-energy Pb 6s states are fully hybridized with the Pb 6p and O/O_H 2p states, forming a strongly covalent Pb-O/OH bond (Figure 4a,b). The low-energy Pb 6s states are little mixed with the O/O_H 2p states and unmixed with the Pb 6p states. In contrast to the Pb-O/OH bond, the O_{2H} 2p states from the Pb-H_2O bond are mixed with both the Pb 6s states at low energy and with the Pb 6s6p states at high energy (Figure 4c). However, the Pb and O_{2H} states only partly overlap, which indicates that the bond interactions of Pb are weaker with H_2O molecules than with surface O atoms and OH groups. This explains why the Pb-H_2O bond lengths of the 3+1 aqua species are 0.10 Å longer than those of the ^{III}Pb-TCS complex.

Metal sorption selectivity of surface sites. All ΔG values of complexation are listed in Table S2 and those of the most stable complexes are plotted in Figure 5. ΔG is a predictor of the affinity of metals for a surface site, and the $\Delta(\Delta G)$ differences between metals provide insight into the metal sorption selectivity of this site. It is important to note that ΔG does not directly inform on the equilibrium distribution between the complexed and uncomplexed metal cations (i.e., [Me-MnO_2]/$[Me]_{aq}$), because complexation reactions depend on the activity of protons in solution. Metal sorption can occur (1) without deprotonation of the surface hydroxyl (SES and DCS, reactions (2) and (4)), (2) with loss of one proton (DES, reaction (3)), and (3) with loss of two protons (TCS, reaction (1)). According to the mass-action law (K~([Me-MnO_2][H^+]^n)/$[Me]_{aq}$), the partitioning of Me between the solution and the solid phase is independent of pH in the first case, is proportional to [H^+] in the second case, and to $[H^+]^2$ in the third case. Equilibrium $[Me\text{-}MnO_2]/[Me]_{aq}$ ratios of metals on the different surface sites as a function of pH are discussed in the next section.

ΔG values follow the order $\Delta G(^{V}Cu) < \Delta G(^{VI}Cu) < \Delta G(Ni) < \Delta G(Zn)$ regardless of the surface site, indicating that Cu would bind preferentially over Ni and Zn to the MnO_2 surface. This result is consistent with Me^{2+} sorption isotherm data fit with the constant capacity model and the CD-MUSIC/triple-layer model, which show that Cu has a higher affinity than Zn and Ni for the TCS and DCS sites.[127] The Pb results are more contrasted as ΔG depends (1) on its hydration state in solution, with ΔG being 10 kcal/mol lower for $Pb(H_2O)_6$ than $Pb(H_2O)_4$ sorption, and (2) on the coordination of the surface complex. In comparision, the difference between $Cu(H_2O)_6$ and $Cu(H_2O)_5$ sorption is 2.9 kcal/mol. Regarding the second factor, the trigonal pyramidal geometry (^{III}Pb) is 4-5 kcal/mol more stable than the seesaw geometry (^{IV}Pb, Table S2). Regarding the first factor, aqua $[Pb(H_2O)_6]^{2+}$ outcompetes all Me cations on all surface sites, whereas $[Pb(H_2O)_4]^{2+}$ has similar affinity for the TCS, DCS, and SES sites than $[Cu(H_2O)_6]^{2+}$, and it is outcompeted by aqua $[Cu(H_2O)_6]^{2+}$ and $[Ni(H_2O)_6]^{2+}$, on the DES site (Figure 5). Since $[Pb(H_2O)_6]^{2+}$ is more abundant than $[Pb(H_2O)_4]^{2+}$ in aqueous solution, according to EXAFS,[100, 102] we conclude that the relative metal sorption affinity for all surface sites decreases in the order Pb > Cu > Ni > Zn. Van Genuchten and Peña[78] interpreted Pb adsorption isotherms at pH 5.5 and differential pair distribution function (d-PDF) analysis to indicate that δ-MnO_2 edges have highest metal selectivity for Pb. Our findings agree with this experimental observation.

Equilibrium distribution of the surface complexes. The predicted equilibrium constants (K) of the surface complexes and the $[Me\text{-}MnO_2]/[Me]_{aq}$ ratios at $5 \leq pH \leq 8$ are given in Table S2, and the $[Me\text{-}MnO_2]/[Me]_{aq}$ ratios at pH 5 and 8 are shown graphically in Figure 6. The $[Me\text{-}MnO_2]/[Me]_{aq}$ ratios decrease in the order DES > TCS > DCS > SES at all pH. Thus, the DES sites are the high-energy sites for the three metals and are occupied first at low surface coverage.

The pK values of the Pb complexes decrease in the order DCS > DES > TCS, in agreement with Pb adsorption data modeled with CD-MUSIC.[128] However, the pK(DCS) - pK (DES) difference is only +0.9, which is within the precision of 1, while the pK(DES) - pK (TCS) = 5.6 difference is significant. The sorption selectivity derived from the $[Pb\text{-}MnO_2]/[Pb]_{aq}$ ratios after application of the mass-action law follows the order DES ≈ TCS > DCS ≈ SES at pH 5 and TCS > DES > DCS ≈ SES at pH > 5 (Figure 6). Since we are interested here in the relative stability of the Pb surface species (i.e., $\Delta(\Delta G)$), the uncertainty regarding the actual solvation state and conformation of the Pb^{2+} aqua ion does not interfere. The similar affinity of Pb for the DES and TCS sites at pH 5 agrees with the

EXAFS results of Takahashi et al.[8] which show that Pb is bonded approximately evenly on the two sites at a Pb/Mn at. ratio of 0.002.

At pH 8, close to the acidity of marine waters, the highest [Me-MnO_2]/$[Me]_{aq}$ ratio of each metal decreases in the order ^{III}Pb-TCS > ^{V}Cu-DES > Ni-DES > Zn-DES (Figure 6b). This order, which corresponds to the affinity sequence of the four metals for MnO_2, parallels their geochemical partitioning between seawater ($[Me]_{aq}$) and marine ferromanganese crusts ([Me-MnO_2]). Pb is enriched ~10^9 times, Cu ~4×10^6 times, Ni ~10^6 times, and Zn ~8×10^5 times in FeMn crusts relative to seawater,[129] and the differences of partitioning can be explained in terms of the binding energy of metals to the MnO_2 surface. Pb(II) is even more enriched than redox-sensitive Co(II) (~8×10^8), which is sequestered as Co(III). The billion-fold enrichment of Pb can be explained by the structure property-energetics relationship of the dehydrated Pb surface complex at the δ-MnO_2-water interface. Although Pb is speciated dominantly as $[PbCl_n]^{2+-n}$/$[PbCO_3]^0$ in seawater instead of $[Pb(H_2O)_6]^{2+}$,[130] this should not change the selectivity sequence because the strong bonding of Pb to the TCS site is driven by the trigonal geometry of the $3O_{2Mn}$ site which matches the stereochemistry of Pb.

Recently, Wegorzewski et al.[31] hypothesized that Ni is incorporated in the layers and Cu is located at the edges of marine phyllomanganates. The uptake modes of Ni and Cu can be rationalized based on their higher affinity for the DES than the TCS sites and their crystal chemical properties. Birnessite crystals grow by lateral extension of the growth layers through the incorporation of MnO_6 octahedra on edge sites. The binding energy of an adatom increases with the number of exposed O ligands, which is two for SES, three for DES, and four for a triple-edge-sharing complex (TES). A TES surface site is unlikely to exist as it is highly reactive and would be rapidly filled by a Mn atom. Thus, crystal growth occurs more likely by adsorption of Mn atoms on DES sites, and it is probably how a Ni-DES complex is incorporated in the MnO_2 layer (DES-INC pathway). This mechanism may explain also how Ni is incorporated in the MnO_2 layer of the MnO_2-$Al(OH)_3$ mixed-layer lithiophorite.[13, 92] In contrast to Ni, steric constraints imposed by the Jahn-Teller distortion of the ^{V}Cu-DES and ^{VI}Cu-DES complexes likely hinder its incorporation in the MnO_2 layer.

CONCLUSION

The main results of this study can be summarized as follows: (1) Pb has the highest affinity for MnO_2 out of the four metals studied, followed by Cu, Ni, and Zn; (2) Ni, Cu, and Zn have a higher affinity for the DES layer edge sites than for the TCS layer surface site; and (3) Pb has a higher affinity for the TCS sites at circumneutral pH and a similar affinity for the TCS and DES sites at acidic pH. Pb uptake on TCS sites may, however, be rapidly limited at increasing surface loading by the density of sites available for sorption. The vacancy sites of δ-MnO_2 and well-crystallized birnessite are usually capped on one side by octahedrally coordinated Mn^{3+} cations, and to a lesser extent by Mn^{2+} cations.[45, 58] Mn^{3+} cations cannot be replaced with Pb as it is strongly bonded to the surface (ΔG = -57.0 kcal/mol). Mn^{2+} cations can be easily replaced (ΔG = -10.8 kcal/mol), yet there are few of them. Overall, this study on the energetics of metal sorption on phyllomanganate complements the EXAFS-based approach.

ASSOCIATED CONTENT

Supporting Information

The Supporting Information is available free of charge on the ACS Publications website at DOI:

Supplementary table and figures (PDF)
Cartesian coordinates of the surface complexes (xlsx)

AUTHOR INFORMATION

Corresponding Author

E-mail: alain.manceau@univ-grenoble-alpes.fr

ORCID

Alain Manceau: 0000-0003-0845-611X
Stephan N. Steinmann: 0000-0002-2777-356X

Notes

The authors declare no competing financial interests.

ACKNOWLEDGEMENTS

The CIMENT infrastructure from the University Grenoble Alpes provided computing resources, and Pierre Girard gave his expertise in parallel scientific processing. Support was provided by the ANR under grant ANR-10-EQPX-27-01.

REFERENCES

(1) Jones, L. H. P.; Milne, A. Birnessite, a new manganese oxide mineral from Aberdeenshire, Scotland. *Min. Mag.* **1956,** *31*, 283-288.

(2) Post, J. E. Manganese oxide minerals: Crystal structures and economic and environmental significance. *Proc. Natl. Acad. Sci. USA* **1999,** *96*, 3447-3454.

(3) Grangeon, S.; Bataillard, P.; Coussy, S. The nature of manganese oxides in soils and their role as scavengers of trace elements: Implications for soil remediation. In *Environmental Soil Remediation and Rehabilitation. Applied Environmental Science and Engineering for a Sustainable Future.*, van Hullebusch, E.; Huguenot, D.; Pechaud, Y.; Simonnot , M. O.; Colombano, S., Eds. Springer, Cham: 2020; pp 399-429.

(4) Frierdich, A.; Catalano, J. G. Distribution and speciation of trace elements in iron and manganese oxide cave deposits *Geochim. Cosmochim. Acta* **2012,** *91*, 240-253.

(5) Isaure, M. P.; Manceau, A.; Geoffroy, N.; Laboudigue, A.; Tamura, N.; Marcus, M. A. Zinc mobility and speciation in soil covered by contaminated dredged sediment using micrometer-scale and bulk-averaging X-ray fluorescence, absorption and diffraction techniques. *Geochim. Cosmochim. Acta* **2005,** *69*, 1173-1198.

(6) Bodei, S.; Manceau, A.; Geoffroy, N.; Baronnet, A.; Buatier, M. Formation of todorokite from vernadite in Ni-rich hemipelagic sediments. *Geochim. Cosmichim. Acta* **2007,** *71*, 5698–5716.

(7) Peacock, C. L.; Sherman, D. M. Crystal-chemistry of Ni in marine ferromanganese crusts and nodules. *Am. Miner.* **2007,** *92*, 1087-1092.

(8) Takahashi, Y.; Manceau, A.; Geoffroy, N.; Marcus, M. A.; Usui, A. Chemical and structural control of the partitioning of Co, Ce, and Pb in marine ferromanganese oxides. *Geochim. Cosmichim. Acta* **2007,** *71*, 984-1008.

(9) Manceau, A.; Kersten, M.; Marcus, M. A.; Geoffroy, N.; Granina, L. Ba and Ni speciation in a nodule of binary Mn oxide phase composition from Lake Baikal. *Geochim. Cosmochim. Acta.* **2007,** *71*, 1967-1981.

(10) Manceau, A.; Lanson, M.; Takahashi, Y. Mineralogy and crystal chemistry of Mn, Fe, Co, Ni, and Cu in a deep-sea Pacific polymetallic nodule. *Am. Miner.* **2014,** *99*, 2068-2083.

(11) Manceau, A.; Tamura, N.; Celestre, R. S.; MacDowell, A. A.; Geoffroy, N.; Sposito, G.; Padmore, H. A. Molecular-scale speciation of Zn and Ni in soil ferromanganese nodules from loess soils of the Mississippi basin. *Environ. Sci. Technol.* **2003,** *37*, 75-80.

(12) Manceau, A.; Marcus, M. A.; Tamura, N.; Proux, O.; Geoffroy, N.; Lanson, B. Natural speciation of Zn at the micrometer scale in a clayey soil using X-ray fluorescence, absorption, and diffraction. *Geochim. Cosmochim. Acta* **2004,** *68*, 2467-2483.

(13) Manceau, A.; Tommaseo, C.; Rihs, S.; Geoffroy, N.; Chateigner, D.; Schlegel, M.; Tisserand, D.; Marcus, M. A.; Tamura, N.; Chen, Z. S. Natural speciation of Mn, Ni and Zn at the micrometer

scale in a clayey paddy soil using X-ray fluorescence, absorption, and diffraction. *Geochim. Cosmochim. Acta* **2005,** *69*, 4007-4034.

(14) Usui, A.; Mita, N. Geochemistry and mineralogy of a modern buserite deposit from a hot spring in hokkaido, Japan. *Clays Clay Miner.* **1995,** *43*, 116-127.

(15) McKeown, D. A.; Post, J. E. Characterization of manganese oxide mineralogy in rock varnish and dendrites using X-ray absorption spectroscopy. *Am. Miner.* **2001,** *86*, 701-713.

(16) Manceau, A.; Lanson, M.; Geoffroy, N. Natural speciation of Ni, Zn, Ba and As in ferromanganese coatings on quartz using X-ray fluorescence, absorption, and diffraction. *Geochim. Cosmochim. Acta* **2007,** *71*, 95-128.

(17) Miller, A. Z.; Dionisio, A.; Braga, M. A. S.; Hernandez-Marine, M.; Afonso, M. J.; Muralha, V. S. F.; Herrera, L. K.; Raabe, J.; Fernandez-Cortes, A.; Cuezva, S., et al. Biogenic Mn oxide minerals coating in a subsurface granite environment. *Chem. Geol.* **2012,** *322*, 181-191.

(18) Frierdich, A. J.; Hasenmueller, E. A.; Catalano, J. G. Composition and structure of nanocrystalline Fe and Mn oxide cave deposits: Implications for trace element mobility in karst systems. *Chem. Geol.* **2011,** *284*, 82-96.

(19) Yu, C. X.; Drake, H.; Mathurin, F. A.; Astrom, M. E. Cerium sequestration and accumulation in fractured crystalline bedrock: The role of Mn-Fe (hydr-)oxides and clay minerals. *Geochim. Cosmochim. Acta* **2017,** *199,* 370-389.

(20) Hochella, M. F.; Kasama, T.; Putnis, A.; Putnis, C. V.; Moore, J. N. Environmentally important, poorly crystalline Fe/Mn hydrous oxides: Ferrihydrite and a possibly new vernadite-like mineral from the Clark Fork River Superfund Complex. *Am. Miner.* **2005,** *90*, 718-724.

(21) Tan, H.; Zhang, G. X.; Heaney, P. J.; Webb, S. M.; Burgos, W. D. Characterization of manganese oxide precipitates from Appalachian coal mine drainage treatment systems. *Appl. Geochem.* **2010,** *25*, 389-399.

(22) Usui, A. Nickel and copper accumulations as essential elements in 10-Å manganite of deep-sea manganese nodules. *Nature* **1979,** *279*, 411-413.

(23) Marcus, M. A.; Manceau, A.; Kersten, M. Mn, Fe, Zn and As speciation in a fast-growing ferromanganese marine nodule. *Geochim. Cosmichim. Acta* **2004,** *68*, 3125-3136.

(24) Peacock, C. L.; Moon, E. M. Oxidative scavenging of thallium by birnessite: Explanation for thallium enrichment and stable isotope fractionation in marine ferromanganese precipitates. *Geochim. Cosmichim. Acta* **2012,** *84*, 297-313.

(25) Kashiwabara, T.; Takahashi, Y.; Marcus, M. A.; Uruga, T.; Tanida, H.; Terada, Y.; Usui, A. Tungsten species in natural ferromanganese oxides related to its different behavior from molybdenum in oxic ocean. *Geochim. Cosmochim. Acta* **2013,** *106*, 364-378.

(26) Kashiwabara, T.; Oishi, Y.; Sakaguchi, A.; Sugiyama, T.; Usui, A.; Takahashi, Y. Chemical processes for the extreme enrichment of tellurium into marine ferromanganese oxides. *Geochim. Cosmochim. Acta* **2014,** *131*, 150-163.

(27) Yang, S. T.; Uesugi, S.; Qin, H. B.; Tanaka, M.; Kurisu, M.; Miyamoto, C.; Kashiwabara, T.; Usui, A.; Takahashi, Y. Comparison of arsenate and molybdate speciation in hydrogenetic ferromanganese nodules. *ACS Earth Space Chem.* **2019,** *3*, 29-38.

(28) Wegorzewski, A. V.; Kuhn, T. The influence of suboxic diagenesis on the formation of Manganese nodules in the Clarion Clipperton nodule belt of the Pacific Ocean. *Marine Geol.* **2014**.

(29) Wegorzewski, A. V.; Kuhn, T.; Dohrmann, R.; Wirth, R.; Grangeon, S. Mineralogical characterization of individual growth structures of Mn-nodules with different Ni+Cu content from central Pacific Ocean. *Am. Miner.* **2015,** *100*, 2497–2508.

(30) Marino, E.; Gonzalez, F. J.; Kuhn, T.; Madureira, P.; Wegorzewski, A. V.; Mirao, J.; Medialdea, T.; Oeser, M.; Miguel, C.; Reyes, J., et al. Hydrogenetic, diagenetic and hydrothermal processes forming ferromanganese crusts in the Canary Island seamounts and their influence in the metal recovery rate with hydrometallurgical methods. *Minerals* **2019,** *9*.

(31) Wegorzewski, A. V.; Grangeon, S.; Webb, S. M.; Heller, C.; Kuhn, T. Mineralogical transformations in polymetallic nodules and the change of Ni, Cu and Co crystal-chemistry upon burial in sediments. *Geochim. Cosmichim. Acta* **2020,** *282*, 19-37.

(32) Takashima, T.; Hashimoto, K.; Nakamura, R. Mechanisms of pH-dependent activity for water oxidation to molecular oxygen by MnO_2 electrocatalyst. *J. Am. Chem. Soc.* **2012,** *134*, 1519-1527.

(33) Huynh, M.; Shi, C. Y.; Billinge, S. J. L.; Nocera, D. G. Nature of activated manganese oxide for oxygen evolution. *J. Am. Chem. Soc.* **2015,** *137*, 14887-14904.

(34) Chen, L.; Ding, J.; Jia, J.; Ran, R.; Zhang, C.; Song, X. Cobalt-doped MnO_2 nanofibers for enhanced propane oxidation. *ACS Appl. Nano Mater.* **2019,** *2*, 4417-4426.

(35) Gao, P.; Chen, Z.; Gong, Y. X.; Zhang, R.; Liu, H.; Tang, P.; Chen, X. H.; Passerini, S.; Liu, J. L. The Role of cation vacancies in electrode materials for enhanced electrochemical energy storage: Synthesis, advanced characterization, and fundamentals. *Adv. Energy Mater.* **2020**, n° 1903780.

(36) Kim, E.; Ma, L. A.; Pickup, D.; Chadwick, A. V.; Younesi, R.; Maughan, P.; Irvine, J. T. S.; Armstrong, A. R. Vacancy enhanced oxygen redox reversibility in P3-type magnesium doped sodium

manganese oxide Na0.67Mg0.2Mn0.8O2. *ACS Appl. Energy Mater.* **2020**, doi-org.inc.bib.cnrs.fr/10.1021/acsaem.0c01352.

(37) Beak, D. G.; Basta, N. T.; Scheckel, K. G.; Traina, S. J. Linking solid phase speciation of Pb sequestered to birnessite to oral Pb bioaccessibility: Implications for soil remediation. *Environ. Sci. Technol.* **2008,** *42*, 779-785.

(38) Peng, Q. C.; Liu, L. H.; Luo, Y.; Zhang, Y. S.; Tan, W. F.; Liu, F.; Suib, S. L.; Qiu, G. H. Cadmium Removal from Aqueous Solution by a Deionization Supercapacitor with a Birnessite Electrode. *ACS Appl. Mater. Inter.* **2016,** *8*, 34405-34413.

(39) Yang, X.; Liu, L. H.; Tan, W. F.; Qiu, G. H.; Liu, F. High-performance Cu^{2+} adsorption of birnessite using electrochemically controlled redox reactions. *J. Hazard. Matter.* **2018,** *354*, 107-115.

(40) Post, J. E.; Veblen, D. R. Crystal structure determinations of synthetic sodium, magnesium, and potassium birnessite using TEM and the Rietveld method. *Am. Miner.* **1990,** *75*, 477-489.

(41) Kuma, K.; Usui, A.; Paplawsky, W.; Gedulin, B.; Arrhenius, G. Crystal structures of synlhetic 7 A and 10 Å manganates substituted by mono- and divalent cations. *Min. Mag.* **1994,** *58*, 425-447.

(42) Drits, V. A.; Silvester, E.; Gorshkov, A. I.; Manceau, A. The structure of synthetic monoclinic Na-rich birnessite and hexagonal birnessite. Part 1. Results from X-ray diffraction and selected area electron diffraction. *Am. Miner.* **1997,** *82*, 946-961.

(43) Silvester, E.; Manceau, A.; Drits, V. A. The structure of synthetic monoclinic Na-rich birnessite and hexagonal birnessite. Part 2. Results from chemical studies and EXAFS spectroscopy. *Am. Miner.* **1997,** *82*, 962-978.

(44) Lanson, B.; Drits, V. A.; Feng, Q.; Manceau, A. Crystal structure determination of synthetic Na-rich birnessite: Evidence for a triclinic one-layer cell. *Am. Miner.* **2002,** *87*, 1662-1671.

(45) Lanson, B.; Drits, V. A.; Silvester, E. J.; Manceau, A. Structure of H-exchanged hexagonal birnessite and its mechanism of formation from Na-rich monoclinic buserite at low pH: New data from X-ray diffraction. *Am. Miner.* **2000,** *85*, 826-835.

(46) Akob, D. M.; Bohu, T.; Beyer, A.; Schaffner, F.; Handel, M.; Johnson, C. A.; Merten, D.; Buchel, G.; Totsche, K. U.; Kusel, K. Identification of Mn(II)-Oxidizing Bacteria from a Low-pH Contaminated Former Uranium Mine. *Appl. Environ. Microbiol.* **2014,** *80*, 5086-5097.

(47) Grangeon, S.; Lanson, B.; Miyata, N.; Tani, Y.; Manceau, A. Structure of nanocrystalline phyllomanganates produced by freshwater fungi. *Am. Miner.* **2010,** *95*, 1608-1616.

(48) Miyata, N.; Tani, Y.; Maruo, K.; Tsuno, H.; Sakata, M.; Iwahori, K. Manganese(IV) oxide production by *Acremonium* sp. strain KR21-2 and extracellular Mn(II) oxidase activity. *App. Environ. Microbiol.* **2006,** *72*, 6467-6473.

(49) Miyata, N.; Tani, Y.; Sakata, M.; Iwahori, K. Microbial manganese oxide formation and interaction with toxic metal ions. *J. Biosci. Bioeng.* **2007,** *104*, 1-8.

(50) Nelson, Y. M.; Lion, L. W.; Ghiorse, W. C.; Shuler, M. L. Production of biogenic Mn oxides by Leprothrix discophora SS-1 in a chemically defined growth medium and evaluation of their Pb adsorption characteristics. *Appl. Environ. Microbiol.* **1999,** *65*, 175-180.

(51) Saratovsky, I.; Gurr, S. J.; Hayward, M. A. The Structure of manganese oxide formed by the fungus Acremonium sp strain KR21-2 *Geochim. Cosmichim. Acta* **2009,** *73*, 3291-3300.

(52) Tebo, B. M.; Bargar, J. R.; Clement, B. G.; Dick, G. J.; Murray, K. J.; Parker, D.; Verity, R.; Webb, S. M. Biogenic manganese oxides: Properties and mechanisms of formation. *Annu. Rev. Earth Planet.. Sci.* **2004,** *32*, 287-328.

(53) Villalobos, M.; Toner, B.; Bargar, J.; Sposito, G. Characterization of the manganese oxide produced by *Pseudomonas putida* strain MnB1. *Geochim. Cosmochim. Acta* **2003,** *67*, 2649-2662.

(54) Webb, S. M.; Tebo, B. M.; Bargar, J. R. Structural characterization of biogenic Mn oxides produced in seawater by the marine *bacillus* sp. strain SG-1. *Am. Miner.* **2005,** *90*, 1342.1357.

(55) Manceau, A.; Drits, V. A.; Silvester, E.; Bartoli, C.; Lanson, B. Structural mechanism of Co(II) oxidation by the phyllomanganate, Na-buserite. *Am. Miner.* **1997,** *82*, 1150-1175.

(56) Tournassat, C.; Charlet, L.; Bosbach, D.; Manceau, A. Arsenic(III) oxidation by birnessite and precipitation of manganese(II) arsenate. *Environ. Sci. Technol.* **2002,** *36*, 493-500.

(57) Villalobos, M.; Lanson, B.; Manceau, A.; Toner, B.; Sposito, G. Structural model for the biogenic Mn oxide produced by *Pseudomonas putida*. *Am. Miner.* **2006,** *91*, 489-502.

(58) Manceau, A.; Marcus, M. A.; Grangeon, S.; Lanson, M.; Lanson, B.; Gaillot, A. C.; Skanthakumar, S.; Soderholm, L. Short-range and long-range order of phyllomanganate nanoparticles determined using high energy X-ray scattering. *J. Appl. Crystallogr.* **2013,** *46*, 193-209.

(59) Kwon, K. D.; Refson, K.; Sposito, G. Zinc surface complexes on birnessite: A density functional theory study *Geochim. Cosmochim. Acta* **2009,** *73*, 1273-1284.

(60) Kwon, K. D.; Refson, K.; Sposito, G. Surface complexation of Pb(II) by hexagonal birnessite nanoparticles. *Geochim. Cosmochim. Acta* **2010,** *74*, 6731-6740.

(61) Kwon, K. D.; Refson, K.; Sposito, G. Understanding the trends in transition metal sorption by vacancy sites in birnessite. *Geochim. Cosmochim. Acta* **2013,** *101*, 222-232.

(62) Cruz-Hernandez, Y.; Villalobos, M.; Marcus, M. A.; Pi-Puig, T.; Zanella, R.; Martinez-Villegas, N. Tl(I) sorption behavior on birnessite and its implications for mineral structural changes. *Geochim. Cosmichim. Acta* **2019,** *248,* 356-369.

(63) Koschinsky, A.; Hein, J. R.; Kraemer, D.; Foster, A. L.; Kuhn, T.; Halbach, P. Platinum enrichment and phase associations in marine ferromanganese crusts and nodules based on a multi-method approach. *Chem. Geol.* **2020,** *539*, n° 119426.

(64) Maeno, M. Y.; Ohashi, H.; Yonezu, K.; Miyazaki, A.; Okaue, Y.; Watanabe, K.; Ishida, T.; Tokunaga, M.; Yokoyama, T. Sorption behavior of the Pt(II) complex anion on manganese dioxide (δ-MnO_2): a model reaction to elucidate the mechanism by which Pt is concentrated into a marine ferromanganese crust. *Miner. Deposita* **2016,** *51*, 211-218.

(65) Matocha, C. J.; Elzinga, E. J.; Sparks, D. L. Reactivity of Pb(II) at the Mn(III,IV) (oxyhydr)oxide-water interface. *Environ. Sci. Technol.* **2001,** *35*, 2967-2972.

(66) Grangeon, S.; Lanson, B.; Lanson, M.; Manceau, A. Crystal structure of Ni-sorbed synthetic vernadite: A powder X-ray diffraction study. *Min. Mag.* **2008,** *72,* 1197-1209.

(67) Grangeon, S.; Manceau, A.; Guilhermet, J.; Gaillot, A. C.; Lanson, M.; Lanson, L. Zn sorption modifies dynamically the layer and interlayer structure of vernadite. *Geochim. Cosmichim. Acta* **2012,** *85*, 302-313.

(68) Yu, Q. Q.; Sasaki, K.; Tanaka, K.; Ohnuki, T.; Hirajima, T. Zinc sorption during bio-oxidation and precipitation of manganese modifies the layer stacking of biogenic birnessite. *Geomicrobiol. J.* **2013,** *30*, 829-839.

(69) Zhao, W.; Tan, W. F.; Feng, X. H.; Liu, F.; Xie, Y. N.; Xie, Z. XAFS studies on surface coordination of Pb^{2+} on birnessites with different average oxidation states. *Colloids Surf. A* **2011,** *379*, 86-92.

(70) Qin, Z. J.; Xiang, Q. J.; Liu, F.; Xiong, J.; Koopal, L. K.; Zheng, L. R.; Ginder-Vogel, M.; Wang, M. X.; Feng, X. H.; Tan, W. F., et al. Local structure of Cu^{2+} in Cu-doped hexagonal turbostratic birnessite and Cu^{2+} stability under acid treatment. *Chem. Geol.* **2017,** *466,* 512-523.

(71) Li, Y.; Liu, F. F.; Xu, X. M.; Liu, Y. W.; Li, Y. Z.; Ding, H. R.; Chen, N.; Yin, H.; Lin, H.; Wang, C. Q., et al. Influence of heavy metal sorption pathway on the structure of biogenic birnessite: Insight from the band structure and photostability. *Geochim. Cosmochim. Acta* **2019,** *256,* 116-134.

(72) Simanova, A. A.; Pena, J. Time-resolved investigation of cobalt oxidation by Mn(III)-rich δ-MnO_2 using quick X-ray absorption spectroscopy. *Environ. Sci. Technol.* **2015,** *49*, 10867-10876.

(73) Villalobos, M.; Bargar, J.; Sposito, G. Mechanisms of Pb(II) sorption on a biogenic manganese oxide. *Environ. Sci. Technol.* **2005,** *39*, 569-576.

(74) Wick, S.; Pena, J.; Voegelin, A. Thallium sorption onto manganese oxides. *Environ. Sci. Technol.* **2019,** *53*, 13168-13178.

(75) Yin, H.; Li, H.; Wang, Y.; Ginder-Vogel, M.; Qiu, G. H.; Feng, X. H.; Zheng, L. R.; Liu, F. Effects of Co and Ni co-doping on the structure and reactivity of hexagonal birnessite. *Chem. Geol.* **2014,** *381*, 10-20.

(76) Yin, H.; Liu, Y.; Koopal, L. K.; Feng, X. H.; Chu, S. Q.; Zhu, M. Q.; Liu, F. High Co-doping promotes the transition of birnessite layer symmetry from orthogonal to hexagonal. *Chem. Geol.* **2015,** *410*, 12-20.

(77) Yu, Q.; Sasaki, K.; Tanaka, K.; Ohnuki, T.; Hirajima, T. Structural factors of biogenic birnessite produced by fungus Paraconiothyrium sp WL-2 strain affecting sorption of Co^{2+}. *Chem. Geol.* **2012,** *312*, 106-113.

(78) van Genuchten, C. M.; Pena, J. Sorption selectivity of birnessite particle edges: a d-PDF analysis of Cd(II) and Pb(II) sorption by δ-MnO_2 and ferrihydrite. *Environ. Sci-Proc. Imp.* **2016,** *18*, 1030-1041.

(79) Toner, B.; Manceau, A.; Webb, S. M.; Sposito, G. Zinc sorption to biogenic hexagonal-birnessite particles within a hydrated bacterial biofilm. *Geochim. Cosmichim. Acta* **2006,** *70*, 27-43.

(80) Liu, J.; Yu, L.; Hu, E. Y.; Guiton, B. S.; Yang, X. Q.; Page, K. Large-Scale Synthesis and Comprehensive Structure Study of δ-MnO_2. *Inorg. Chem.* **2018,** *57*, 6873-6882.

(81) Holguera, J. G.; Etui, I. D.; Jensen, L. H. S.; Pena, J. Contaminant loading and competitive access of Pb, Zn and Mn(III) to vacancy sites in biogenic MnO_2. *Chem. Geol.* **2018,** *502*, 76-87.

(82) Yin, H.; Feng, X. H.; Tan, W. F.; Koopal, L. K.; Hu, T. D.; Zhu, M. Q.; Liu, F. Structure and properties of vanadium(V)-doped hexagonal turbostratic birnessite and its enhanced scavenging of Pb^{2+} from solutions. *J. Hazard. Matter.* **2015,** *288*, 80-88.

(83) Grangeon, S.; Fernandez-Martinez, A.; Claret, F.; Marty, N.; Tournassat, C.; Warmont, F.; Gloter, A. In-situ determination of the kinetics and mechanisms of nickel adsorption by nanocrystalline vernadite. *Chem. Geol.* **2017,** *459*, 24-31.

(84) Suzuki, K.; Kato, T.; Fuchida, S.; Tokoro, C. Removal mechanisms of cadmium by δ-MnO_2 in adsorption and coprecipitation processes at pH 6. *Chem. Geol.* **2020,** *550*, n° 119744.

(85) Qin, H. B.; Uesugi, S.; Yang, S. T.; Tanaka, M.; Kashiwabara, T.; Itai, T.; Usui, A.; Takahashi, Y. Enrichment mechanisms of antimony and arsenic in marine ferromanganese oxides: Insights from the structural similarity. *Geochim. Cosmichim. Acta* **2019,** *257*, 110-130.

(86) Peacock, C. L.; Sherman, D. M. Sorption of Ni by birnessite: Equilibrium controls on Ni in seawater. *Chem. Geol.* **2007,** *238*, 94-106.

(87) Peacock, C. L. Physiochemical controls on the crystal-chemistry of Ni in birnessite: Genetic implications for ferromanganese precipitates. *Geochim. Cosmochim. Acta* **2009,** *73*, 3568-3578.

(88) Pena, J.; Kwon, K. D.; Refson, K.; Bargar, J. R.; Sposito, G. Mechanisms of nickel sorption by a bacteriogenic birnessite. *Geochim. Cosmichim. Acta* **2010,** *74*, 3076-3089.

(89) Yin, H.; Tan, W. F.; Zheng, L. R.; Cui, H. J.; Qiu, G. H.; Liu, F.; Feng, X. H. Characterization of Ni-rich hexagonal birnessite and its geochemical effects on aqueous Pb^{2+}/Zn^{2+} and As(III). *Geochim. Cosmichim. Acta* **2012,** *93*, 47-62.

(90) Simanova, A. A.; Kwon, K. D.; Bone, S. E.; Bargar, J. R.; Refson, K.; Sposito, G.; Pena, J. Probing the sorption reactivity of the edge surfaces in birnessite nanoparticles using nickel(II). *Geochim. Cosmichim. Acta* **2015,** *164*, 191-204.

(91) Sorensen, J. V.; Gueguen, B.; Stewart, B. D.; Pena, J.; Rouxel, O.; Toner, B. M. Large nickel isotope fractionation caused by surface complexation reactions with hexagonal birnessite. *Chem. Geol.* **2020,** *537*, n° 119481.

(92) Manceau, A.; Tamura, N.; Marcus, M. A.; MacDowell, A. A.; Celestre, R. S.; Sublett, R. E.; Sposito, G.; Padmore, H. A. Deciphering Ni sequestration in soil ferromanganese nodules by combining X-ray fluorescence, absorption and diffraction at micrometer scales of resolution. *Am. Miner.* **2002,** *87*, 1494-1499.

(93) Wang, Y. H.; Benkaddour, S.; Marafatto, F. F.; Pena, J. Diffusion- and pH-dependent reactivity of layer-type MnO_2: Reactions at particle edges versus vacancy sites. *Environ. Sci. Technol.* **2018,** *52*, 3476-3485.

(94) Spadini, L.; Manceau, A.; Schindler, P. W.; Charlet, L. Structure and stability of Cd^{2+} surface complexes on ferric oxides. I. Results from EXAFS spectroscopy. *J. Colloid Interface Sci.* **1994,** *168*, 73-86.

(95) Blumberger, J.; Bernasconi, L.; Tavernelli, I.; Vuilleumier, R.; Sprik, M. Electronic structure and solvation of copper and silver ions: A theoretical picture of a model aqueous redox reaction. *J. Am. Chem. Soc.* **2004,** *126*, 3928-3938.

(96) Tonkin, J. W.; Balistrieri, L. S.; Murray, J. W. Modeling sorption of divalent metal cations on hydrous manganese oxide using the diffuse double layer model. *App. Geochem.* **2004,** *19*, 29-53.

(97) Appelo, C. A. J.; Postma, D. A consistent model for surface complexation on birnessite (-MnO2) and its application to a column experiment. *Geochim. Cosmochim. Acta* **1999,** *63*, 3039-3048.

(98) Conway, B. E. *Ionic Hydration in Chemistry and Biophysics*. Elsevier: Amsterdam: 1981.

(99) Shimoni-Livny, L.; Glusker, J. P.; Bock, C. W. Lone pair functionality in divalent lead compounds. *Inorg. Chem.* **1998,** *37*, 1853-1867.

(100) Etschmann, B. E.; Mei, Y.; Liu, W.; Sherman, D.; Testemale, D.; Muller, H.; Rae, N.; Kappen, P.; Brugger, J. The role of Pb(II) complexes in hydrothermal mass transfer: An X-ray absorption spectroscopic study. *Chem. Geol.* **2018,** *502*, 88-106.

(101) Akibo-Betts, G.; Barran, P. E.; Puskar, L.; Duncombe, B.; Cox, H.; Stace, A. J. Stable $[Pb(ROH)_N]^{2+}$ complexes in the gas phase: Softening the base to match the Lewis acid. *J. Am. Chem. Soc.* **2002,** *124*, 9257-9264.

(102) Persson, I.; Lyczko, K.; Lundberg, D.; Eriksson, L.; Płaczek, A. Coordination chemistry study of hydrated and solvated lead(II) ions in solution and solid state. *Inorg. Chem.* **2011,** *50*, 1058−1072.

(103) Leon-Pimentel, C. I.; Martinez-Jimenez, M.; Saint-Martin, H. Study of the elusive hydration of Pb^{2+} from the gas phase to the liquid aqueous solution: Modeling the hemidirected solvation with a polarizable MCDHO force-field. *J. Phys. Chem. B* **2019,** *123*, 9155-9166.

(104) Adamo, C.; Barone, V. Toward reliable density functional methods without adjustable parameters: The PBE0 model. *J. Chem. Phys.* **1999,** *110*, 6158-6170.

(105) Perdew, J. P.; Ernzerhof, M. Rationale for mixing exact exchange with density functional approximations. *J. Chem. Phys.* **1996,** *105*, 9982-9985.

(106) Perdew, J. P.; Burke, K.; Ernzerhof, M. Generalized gradient approximation made simple. *Phys. Rev. Lett.* **1996,** *77*, 3865-3868.

(107) Bühl, M.; Reimann, C.; Pantazis, D. A.; Bredow, T.; Neese, F. Geometries of third-row transition-metal complexes from density-functional theory. *J. Chem. Theor. Comput.* **2008,** *4*, 1449-1459.

(108) Weigend, F.; Ahlrichs, R. Balanced basis sets of split valence, triple zeta valence and quadruple zeta valence quality for H to Rn: Design and assessment of accuracy. *Phys. Chem. Chem. Phys.* **2005,** *7*, 3297-3305.

(109) Weigend, F. Accurate Coulomb-fitting basis sets for H to Rn. *Phys. Chem. Chem. Phys.* **2006,** *8*, 1057-1065.

(110) Grimme, S.; Ehrlich, S.; Goerigk, L. Effect of the damping function in dispersion corrected density functional theory. *J. Comput. Chem.* **2011,** *32*, 1456-1465.

(111) Marenich, A. V.; Cramer, C. J.; Truhlar, D. G. Universal solvation model based on solute electron density and on a continuum model of the solvent defined by the bulk dielectric constant and atomic surface tensions. *Phys. Chem. B* **2009,** *113*, 6378-6396.

(112) Mirzaei, S.; Ivanov, M. V.; Timerghazin, Q. K. Improving performance of the SMD solvation model: Bondi radii improve predicted aqueous solvation free energies of ions and pK_a values of thiols. *J. Phys. Chem. A* **2019,** *123*, 9498-9504.

(113) Marenich, A. V.; Cramer, C. J.; Truhlar, D. G. Universal solvation model based on solute electron density and on a continuum model of the solvent defined by the bulk dielectric constant and atomic surface tensions. *J. Phys. Chem. B* **2009,** *113*, 6378-6396.

(114) Kelly, C. P.; Cramer, C. J.; Truhlar, D. G. Aqueous solvation free energies of ions and ion-water clusters based on an accurate value for the absolute aqueous solvation free energy of the proton. *J. Phys. Chem. B.* **2006,** *110*, 16066–16081.

(115) Besora, M.; Vidossich, P.; Lledos, A.; Ujaque, G.; Maseras, F. Calculation of reaction free energies in solution: A comparison of current approaches. *J. Phys. Chem. A* **2018,** *122*, 1392-1399.

(116) Neese, F. Software update: the ORCA program system, version 4.0. *WIREs Comput. Mol. Sci.* **2017**, e1327.

(117) Smith, S. M.; Martell, A. E. *Critical Stability Constants. Vol. 4: Inorganic Complexes*. Plenum Press: 1976; p 257.

(118) Manceau, A.; Lanson, B.; Drits, V. A. Structure of heavy metal sorbed birnessite. Part III. Results from powder and polarized extended X-ray absorption fine structure spectroscopy. *Geochim. Cosmochim. Acta.* **2002,** *66*, 2639-2663.

(119) Toner, B.; Manceau, A.; Marcus, M. A.; Millet, D. B.; Sposito, G. Zinc sorption by a bacterial biofilm. *Environ. Sci. Technol.* **2005,** *39*, 8288-8294.

(120) Zhu, M. Q.; Ginder-Vogel, M.; Sparks, D. L. Ni(II) sorption on biogenic Mn-oxides with varying Mn octahedral layer structure. *Environ. Sci. Technol.* **2010,** *44*, 4472–4478.

(121) Zhu, M. Q.; Ginder-Vogel, M.; Parikh, S. J.; Feng, X. H.; Sparks, D. L. Cation effects on the layer structure of biogenic Mn-oxides. *Environ. Sci. Technol.* **2010,** *44*, 4465–4471.

(122) Pena, J.; Bargar, J. R.; Sposito, G. Copper sorption by the edge surfaces of synthetic birnessite nanoparticles. *Chem. Geol.* **2015,** *396*, 196-207.

(123) Sherman, D. M.; Peacock, C. L. Surface complexation of Cu on birnessite (δ-MnO_2): Controls on Cu in the deep ocean. *Geochim. Cosmochim. Acta.* **2010,** *74*, 6721-6730.

(124) Little, S. H.; Sherman, D. M.; Vance, D.; Hein, J. R. Molecular controls on Cu and Zn isotopic fractionation in Fe–Mn crusts. *Earth Planet. Sci. Lett.* **2014,** *396*, 213-222.

(125) Manceau, A.; Nagy, K. L. Comment on "Molecular controls on Cu and Zn isotopic fractionation in Fe–Mn crusts" by Little et al. *Earth Planet. Sci. Lett.* **2015,** *411*, 310-312.

(126) Sherman, D. M.; Little, S. H. Isotopic disequilibrium of Cu in marine ferromanganese crusts: Evidence from ab initio predictions of Cu isotope fractionation on sorption to birnessite. *Earth. Planet. Sci. Lett.* **2020,** *549*, n° 116540.

(127) Li, Y.; Zhao, X.; Wu, J.; Gu, X. Surface complexation modeling of divalent metal cation adsorption on birnessite. *Chem. Geol.* **2020,** *551*, n° 119774.

(128) Zhao, W.; Tan, W. F.; Wang, M. X.; Xiong, J.; Liu, F.; Weng, L. P.; Koopal, L. K. CD-MUSIC-EDL modeling of Pb^{2+} adsorption on birnessites: Role of vacant and edge sites. *Environ. Sci. Technol.* **2018,** *52*, 10522-10531.

(129) Hein, J. R.; Koschinsky, A. Deep-Ocean ferromanganese crusts and nodules. In *Treatise on Geochemistry*, Holland, H. D.; Turekian, K. K., Eds. Oxford: Elsevier: 2014; Vol. 13, pp 273-291.

(130) Byrne, R. H. Inorganic speciation of dissolved elements in seawater: the influence of pH on concentration ratios. *Geochem. Trans.* **2002,** *3*, 11-16.

FIGURE LEGENDS

Figure 1. **a**) Polyhedral representation of the Mn_6V model with a Mn(IV) vacancy charge-compensated by two protons bound to unsaturated O ions (O_{2Mn}) bordering the vacancy on each side of the layer. **b-e**) Geometry-optimized Ni-TCS, Ni-DCS, Ni-DES, and Ni-SES complexes. **f**) Geometry-optimized Cu-TCS complex with a five-fold coordination.

Figure 2. Geometry-optimized coordinations of Pb(II) to water molecules. **a**) six-fold coordination. **b**) Seesaw geometry.[99] **c**) 3+1 geometry.[101] The Pb-O distances are in angstrom.

Figure 3. Geometry-optimized Pb complexes. **a**) ^{IV}Pb-DCS complex with two solvation water molecules. **b**) ^{VI}Pb-TCS complex. **c**) ^{III}Pb-TCS complex with three solvation water molecules. **d**) ^{III}Pb-TCS complex. **e**) ^{IV}Pb-DCS complex. **f**) ^{III}Pb-DCS complex. **g**) ^{IV}Pb-DES., **h**) ^{III}Pb-DES. **i**) ^{IV}Pb-SES. **j**) ^{III}Pb-SES. ΔG values in kcal/mol are given in parenthesis for the sorption of $[Pb(H_2O)_6]^{2+}$.

Figure 4. Electronic density of states in the valence band region of the Pb-O bond for the ^{III}Pb-TCS complex (**a**), the Pb-O and Pb-OH bonds for the ^{IV}Pb-DES complex (**b**), and the Pb-H_2O bond for the ^{IV}Pb-DES complex (**c**). The HOMO values are the energies of the highest occupied molecular orbitals. The peak arrowed in (**b**) corresponds to the O bonding with H. On top, polyhedral representation of the ^{III}Pb-TCS and ^{IV}Pb-DES complexes.

Figure 5. Gibbs free energy of complexation (ΔG) of the Me^{2+} aqua ions on the Mn_6V nanolayer. For Pb^{2+}, free energies are given for sorption of the six-fold aqua species ($Pb(H_2O)_6$) (**a**), and for the seesaw four-fold species ($Pb(H_2O)_4$) (**b**). $\Delta G(Pb(H_2O)_4) - \Delta G(Pb(H_2O)_6) = 10$ kcal/mol. The Pb coordination of the surface complexes is always three-fold (i.e., ^{III}Pb-TCS, ^{III}Pb-DCS, ^{III}Pb-DES, and ^{III}Pb-SES).

Figure 6. Equilibrium molar ratios of the concentration of complexed Me^{2+} ([Me-MnO_2]) to aqueous Me^{2+} ($[Me]_{aq}$) at pH 5 and 8.

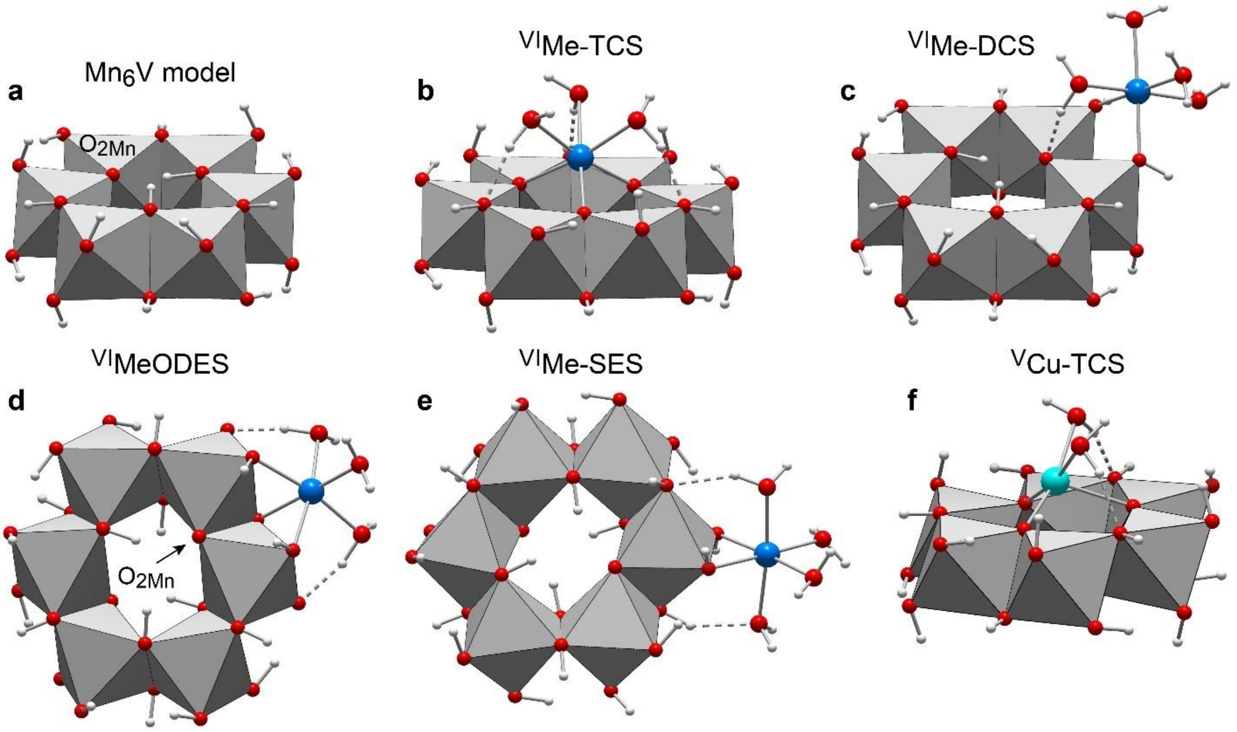

Figure 1

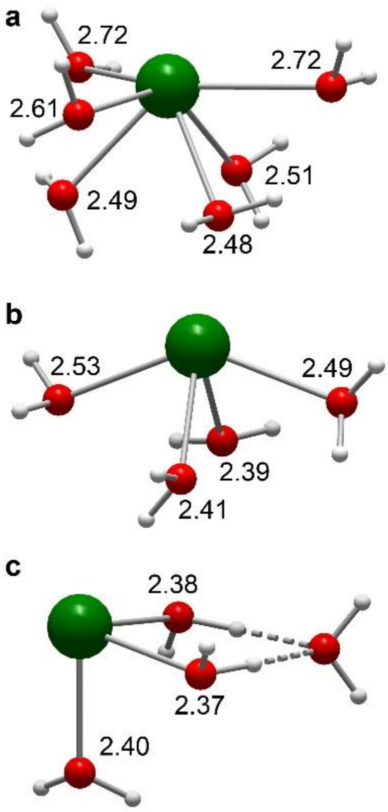

Figure 2

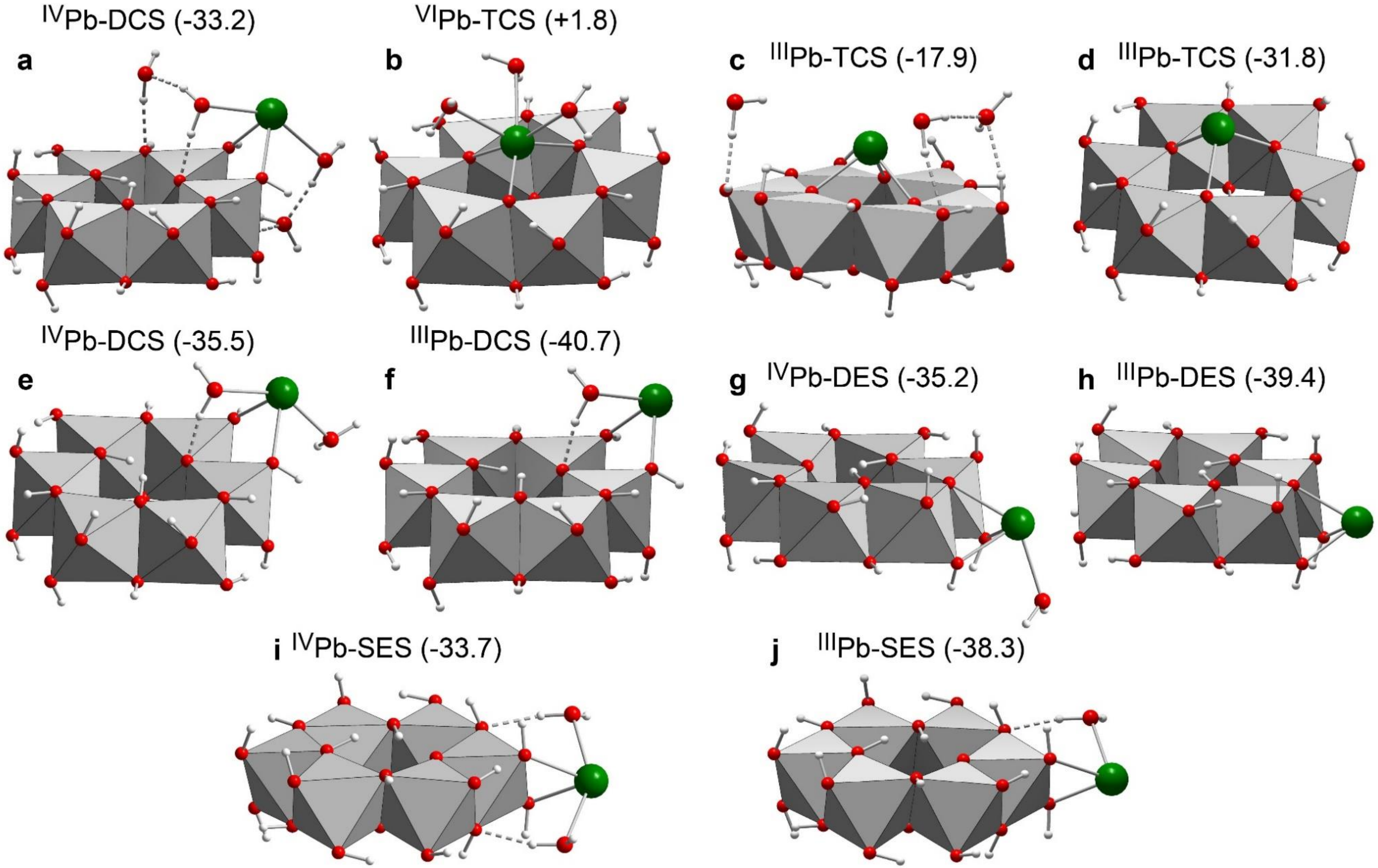
^{IV}Pb-DCS (-33.2)
a
^{VI}Pb-TCS (+1.8)
b
c
^{III}Pb-TCS (-17.9)
d
^{III}Pb-TCS (-31.8)
^{IV}Pb-DCS (-35.5)
e
^{III}Pb-DCS (-40.7)
f
g
^{IV}Pb-DES (-35.2)
h
^{III}Pb-DES (-39.4)
i
^{IV}Pb-SES (-33.7)
j
^{III}Pb-SES (-38.3)

Figure 3

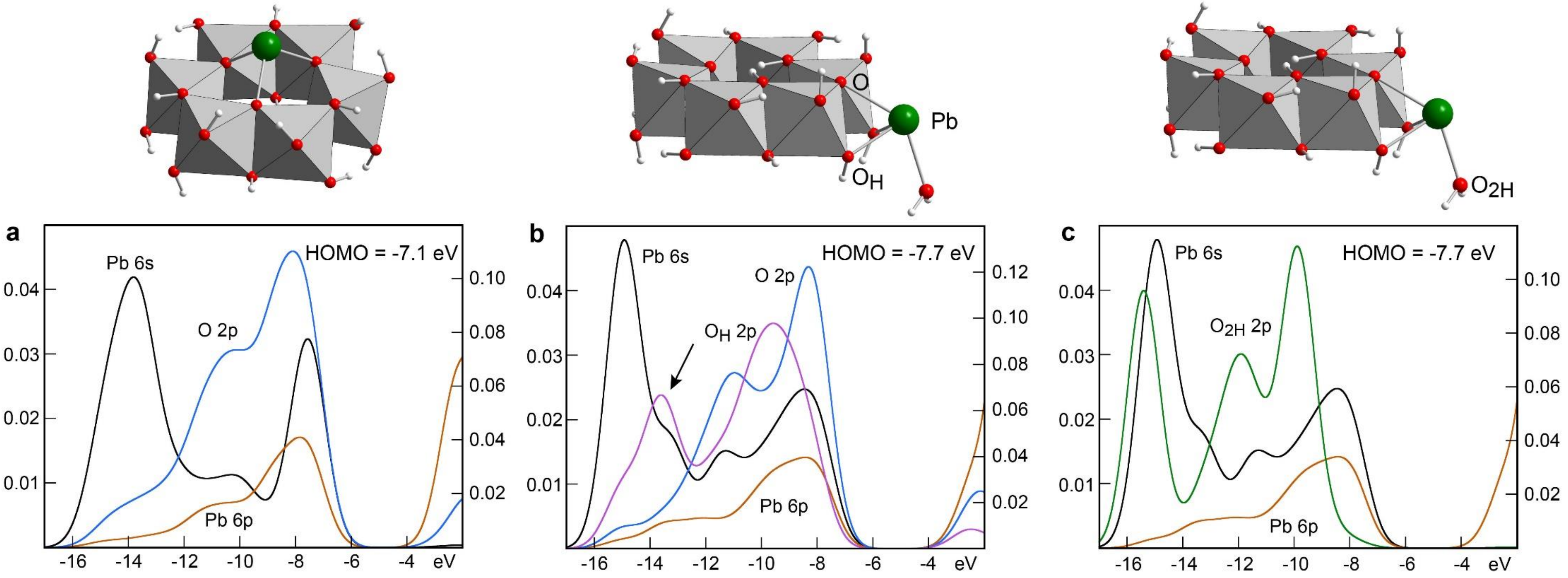
O
Pb
O$_H$
O$_{2H}$
a
Pb 6s
HOMO = -7.1 eV
O 2p
Pb 6p
0.04
0.03
0.02
0.01
0.10
0.08
0.06
0.04
0.02
-16
-14
-12
-10
-8
-6
-4
eV
b
Pb 6s
HOMO = -7.7 eV
O 2p
O$_H$ 2p
Pb 6p
0.04
0.03
0.02
0.01
0.12
0.10
0.08
0.06
0.04
0.02
-16
-14
-12
-10
-8
-6
-4
eV
c
Pb 6s
HOMO = -7.7 eV
O$_{2H}$ 2p
Pb 6p
0.04
0.03
0.02
0.01
0.10
0.08
0.06
0.04
0.02
-16
-14
-12
-10
-8
-6
-4
eV

Figure 4

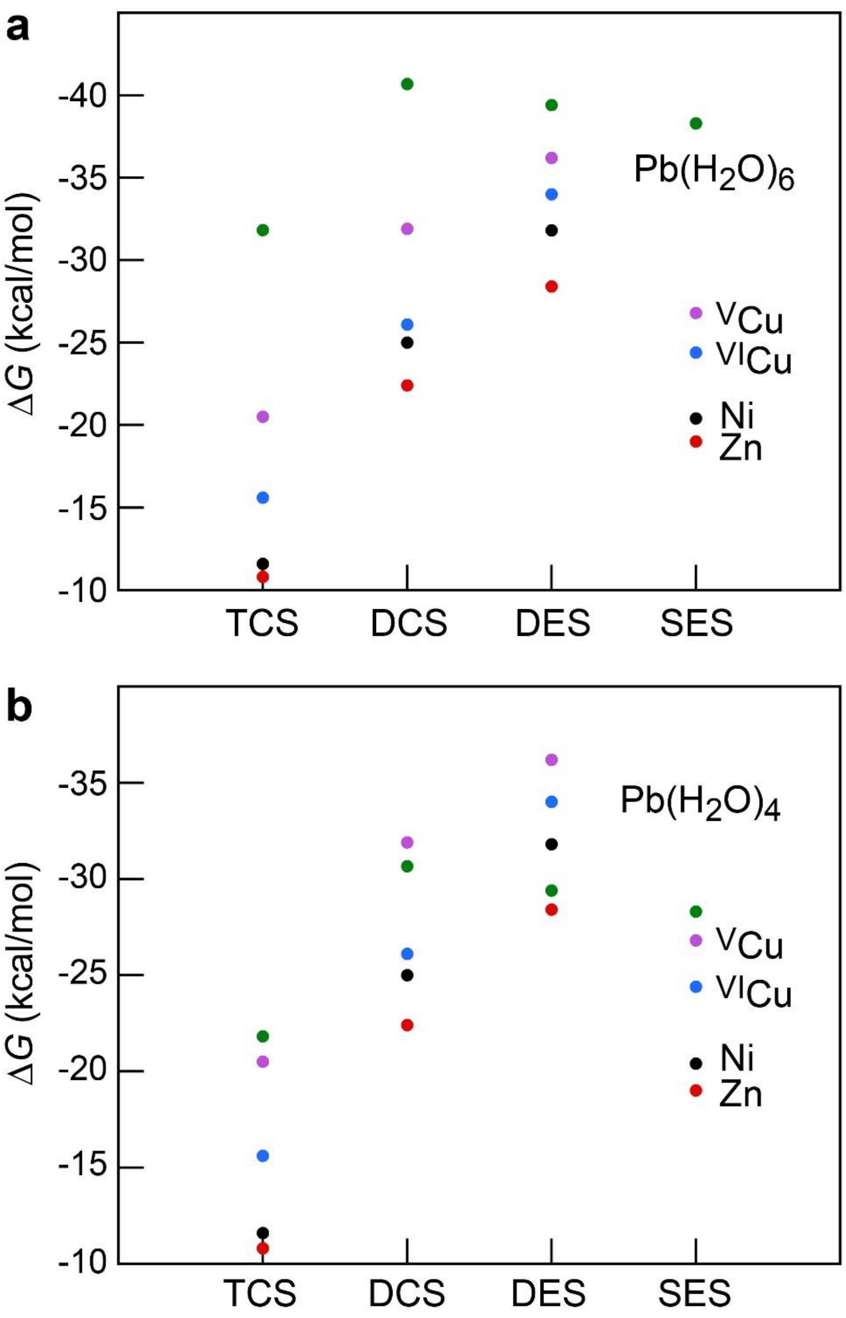
a
-40
-35
-30
-25
-20
-15
-10
ΔG (kcal/mol)
Pb(H2O)6
VCu
VICu
Ni
Zn
TCS
DCS
DES
SES
b
-35
-30
-25
-20
-15
-10
ΔG (kcal/mol)
Pb(H2O)4
VCu
VICu
Ni
Zn
TCS
DCS
DES
SES

Figure 5

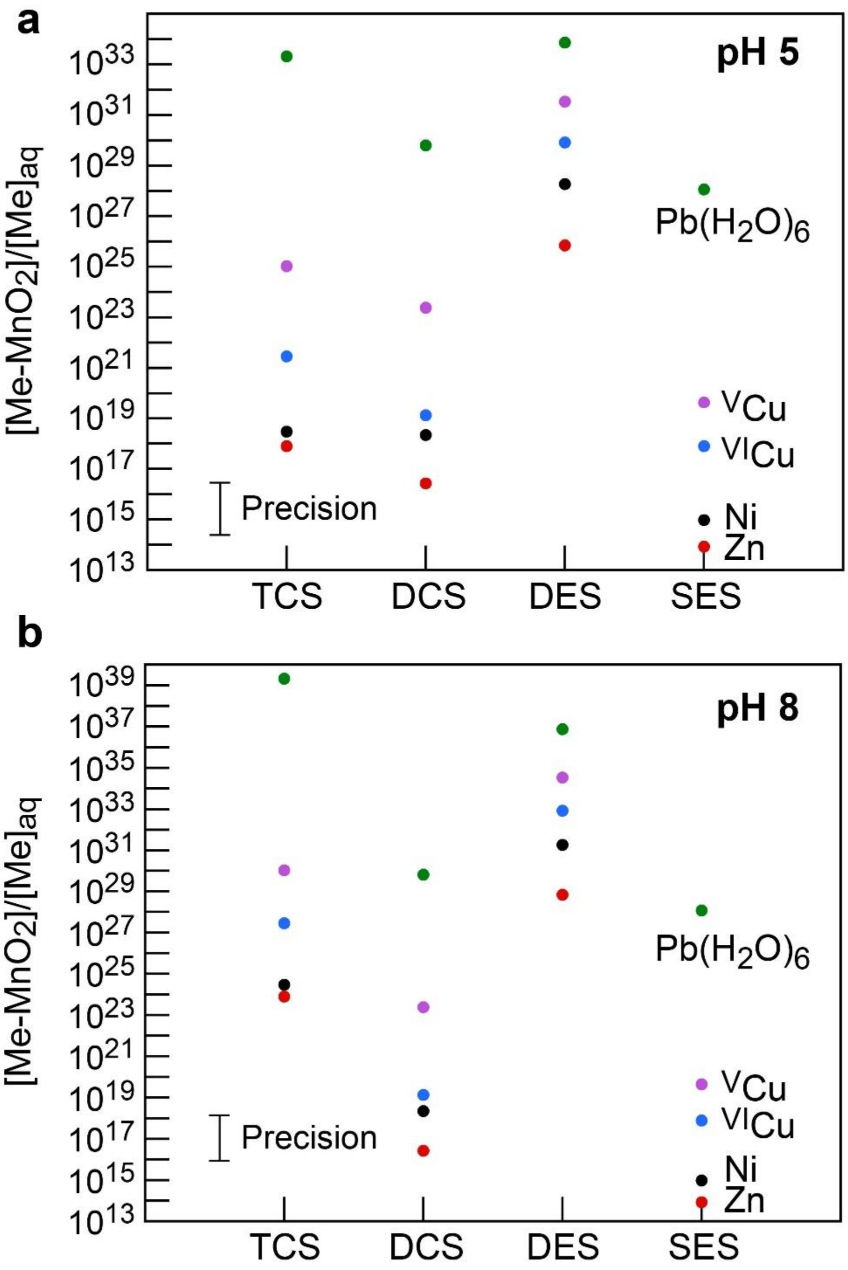
a
pH 5
10^{33}
10^{31}
10^{29}
10^{27}
10^{25}
10^{23}
10^{21}
10^{19}
10^{17}
10^{15}
10^{13}
[Me-MnO2]/[Me]aq
Precision
Pb(H2O)6
VCu
VICu
Ni
Zn
TCS
DCS
DES
SES
b
pH 8
10^{39}
10^{37}
10^{35}
10^{33}
10^{31}
10^{29}
10^{27}
10^{25}
10^{23}
10^{21}
10^{19}
10^{17}
10^{15}
10^{13}
[Me-MnO2]/[Me]aq
Precision
Pb(H2O)6
VCu
VICu
Ni
Zn
TCS
DCS
DES
SES

Figure 6

The Nature of High and Low Affinity Metal Surface Sites on Birnessite Nanosheets

Alain Manceau*[a] and Stephan N. Steinmann[b]

[a] Univ. Grenoble Alpes, CNRS, ISTerre, CS 40700, 38058 Grenoble, France

[b] Univ. Lyon, ENS de Lyon, CNRS, Laboratoire de Chimie, 69342 Lyon, France

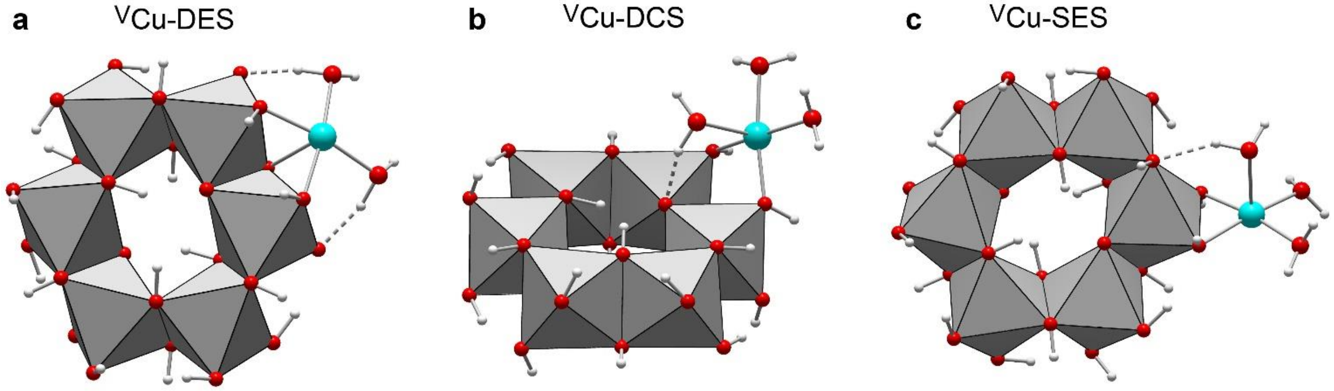

Fig. S1. Geometry-optimized Cu-DES (**a**), Cu-DCS (**b**), and Cu-SES (**c**) complexes with a five-fold coordination.

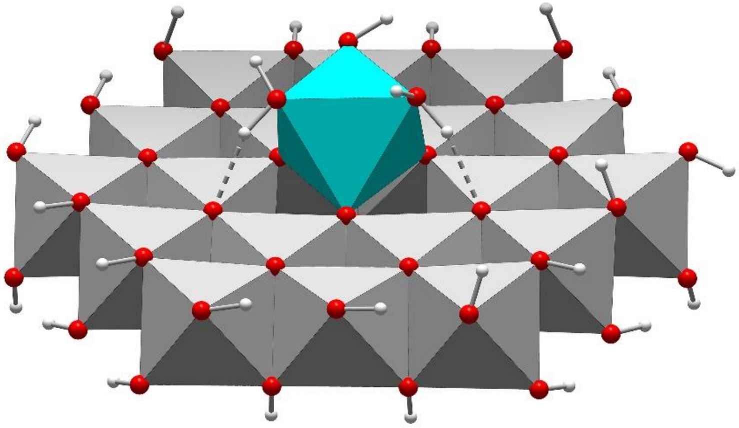

Fig. S2. Geometry-optimized Ni($3O_{2Mn}3H_2O$)-TCS complex on a $Mn_{18}V$ layer. The three water molecules from the Ni-TCS complex are H-bonded to three O_{3M} surface oxygens.

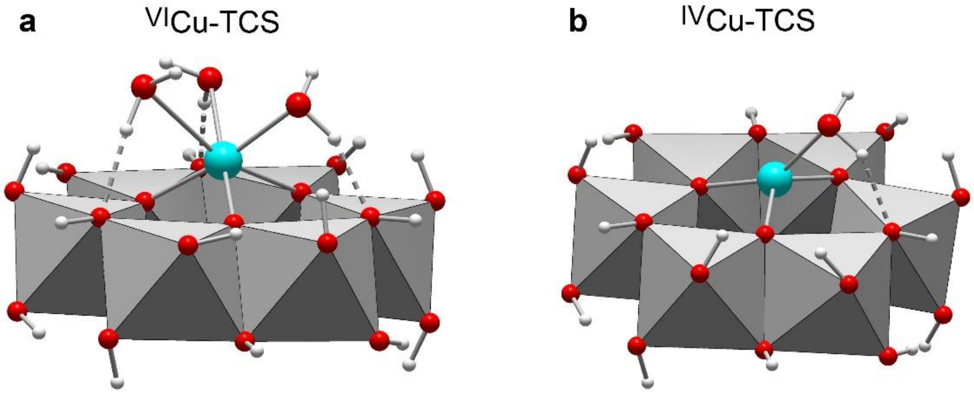

Fig. S3. Geometry-optimized Cu(3O_{2Mn}3H_2O)-TCS (**a**) and Cu(3$O_{2Mn}H_2O$)-TCS (**b**) complexes.

Table S1. Calculated and experimental first hydrolysis contants

Reaction	**Calculated Δ*G***	**Calculated p*K*$_a$**	**Experimental p*K*$_a$**
$Mn(H_2O)_6 \rightarrow [Mn(H_2O)_5OH]^+ + H^+$	15.44 kcal/mol	11.3	10.6
$Ni(H_2O)_6 \rightarrow [Ni(H_2O)_5OH]^+ + H^+$	15.50 kcal/mol	11.4	9.9
$Zn(H_2O)_6 \rightarrow [Zn(H_2O)_5OH]^+ + H^+$	12.47 kcal/mol	9.1	9.0

Table S2. Coordination, interatomic distances (Å), Gibbs free energies of complexation (kcal/mol), equilibrium constants, and $[Me\text{-}MnO_2]/[Me]_{aq}$ ratios at pH 5-8 of geometry-optimized surface complexes.

Code name	**Coordination**	**Complex**	**<Me-O> Cu-Oeq**	**Std**	**<Me-H2O> Cu-Oax**	**Std**	**<Me-Mn>**	**Std**	**Δ*G***	***K***	**p*K***	**pH 5**	**pH 6**	**pH 7**	**pH 8**
$Ni(3O_{2Mn}3H_2O)$-TCS	$Ni(3O_{2Mn}3H_2O)$	Ni-TCS	2.05	0.02	2.14	0.01	3.50	0.04	-11.56	2.98E+08	8.5	2.98E+18	2.98E+20	2.98E+22	2.98E+24
$Ni(2O_{Mn}4H_2O)$-DCS	$Ni(2O_{Mn}4H_2O)$	Ni-DCS	2.03	0.00	2.11	0.01	3.49	0.00	-25.03	2.22E+18	18.3	2.22E+18	2.22E+18	2.22E+18	2.22E+18
$Ni(1O_{2Mn}2O_{Mn}3H_2O)$-DES	$Ni(1O_{2Mn}2O_{Mn}3H_2O)$	Ni-DES	2.07	0.03	2.06	0.01	2.91	0.01	-31.76	1.91E+23	23.3	1.91E+28	1.91E+29	1.91E+30	1.91E+31
$Ni(2O_{Mn}4H_2O)$-SES	$Ni(2O_{Mn}4H_2O)$	Ni-SES	2.03	0.01	2.08	0.03	2.96	-	-20.44	9.61E+14	15.0	9.61E+14	9.61E+14	9.61E+14	9.61E+14
$Cu(3O_{2Mn}3H_2O)$-TCS	$Cu(3O_{2Mn}3H_2O)$	^{VI}Cu-TCS	2.00	0.06	2.42	0.14	3.47	0.10	-15.64	2.91E+11	11.5	2.91E+21	2.91E+23	2.91E+25	2.91E+27
$Cu(2O_{Mn}4H_2O)$-DCS	$Cu(2O_{Mn}4H_2O)$	^{VI}Cu-DCS	1.99	0.04	2.34	0.00	3.43	0.00	-26.10	1.35E+19	19.1	1.35E+19	1.35E+19	1.35E+19	1.35E+19
$Cu(1O_{2Mn}2O_{Mn}3H_2O)$-DES	$Cu(1O_{2Mn}2O_{Mn}3H_2O)$	^{VI}Cu-DES	1.99	0.02	2.33	0.08	3.00	0.01	-34.00	8.36E+24	24.9	8.36E+29	8.36E+30	8.36E+31	8.36E+32
$Cu(2O_{Mn}4H_2O)$-SES	$Cu(2O_{Mn}4H_2O)$	^{VI}Cu-SES	1.98	0.02	2.43	0.10	2.93	-	-24.42	7.94E+17	17.9	7.94E+17	7.94E+17	7.94E+17	7.94E+17
$Cu(3O_{2Mn}2H_2O)$-TCS	$Cu(3O_{2Mn}2H_2O)$	^{V}Cu-TCS	1.99	0.06	2.21	-	3.44	0.06	-20.50	1.06E+15	15.0	1.06E+25	1.06E+27	1.06E+29	1.06E+30
$Cu(2O_{Mn}3H_2O)$-DCS	$Cu(2O_{Mn}3H_2O)$	^{V}Cu-DCS	1.97	0.03	2.25	-	3.40	0.00	-31.90	2.41E+23	23.4	2.41E+23	2.41E+23	2.41E+23	2.41E+23
$Cu(1O_{2Mn}2O_{Mn}2H_2O)$-DES	$Cu(1O_{2Mn}2O_{Mn}2H_2O)$	^{V}Cu-DES	1.97	0.01	2.32	-	2.93	0.01	-36.20	3.43E+26	26.5	3.43E+31	3.43E+32	3.43E+33	3.43E+34
$Cu(2O_{Mn}3H_2O)$-SES	$Cu(2O_{Mn}3H_2O)$	^{V}Cu-SES	1.97	0.02	2.25	-	2.94	0.00	-26.80	4.41E+19	19.6	4.41E+19	4.41E+19	4.41E+19	4.41E+19
$Zn(3O_{2Mn}3H_2O)$-TCS	$Zn(3O_{2Mn}3H_2O)$	Zn-TCS	2.06	0.01	2.20	0.02	3.48	0.05	-10.78	7.98E+07	7.9	7.98E+17	7.98E+19	7.98E+21	7.98E+23
$Zn(2O_{Mn}4H_2O)$-DCS	$Zn(2O_{Mn}4H_2O)$	Zn-DCS	2.05	0.00	2.13	0.01	3.51	0.00	-22.41	2.67E+16	16.4	2.67E+16	2.67E+16	2.67E+16	2.67E+16
$Zn(1O_{2Mn}2O_{Mn}3H_2O)$-DES	$Zn(1O_{2Mn}2O_{Mn}3H_2O)$	Zn-DES	2.16	0.10	2.08	0.01	3.01	0.01	-28.43	6.91E+20	20.8	6.91E+25	6.91E+26	6.91E+27	6.91E+28
$Zn(2O_{Mn}4H_2O)$-SES	$Zn(2O_{Mn}4H_2O)$	Zn-SES	2.07	0.02	2.13	0.07	3.01	-	-19.00	8.45E+13	13.9	8.45E+13	8.45E+13	8.45E+13	8.45E+13
$Pb(3O_{2Mn})$-TCS	$Pb(3O_{2Mn})$	^{III}Pb-TCS	2.29	0.01	-	-	3.71	0.06	-31.82	2.11E+23	23.3	2.11E+33	2.11E+35	2.11E+37	2.11E+39
$Pb(2O_{Mn}H_2O)$-DCS	$Pb(2O_{Mn}H_2O)$	^{III}Pb-DCS	2.30	0.01	2.36	-	3.84	0.00	-40.67	6.48E+29	29.8	6.48E+29	6.48E+29	6.48E+29	6.48E+29
$Pb(2O_{Mn}2H_2O)$-DCS	$Pb(2O_{Mn}2H_2O)$	^{IV}Pb-DCS	2.31	0.00	2.54	0.07	3.88	0.00	-35.46	9.83E+25	26.0	9.83E+25	9.83E+25	9.83E+25	9.83E+25
$Pb(1O_{2Mn}2O_{Mn})$-DES	$Pb(1O_{2Mn}2O_{Mn})$	^{III}Pb-DES	2.36	0.02	-	-	3.23	0.01	-39.39	7.47E+28	28.9	7.47E+33	7.47E+34	7.47E+35	7.47E+36
$Pb(1O_{2Mn}2O_{Mn}H_2O)$-DES	$Pb(1O_{2Mn}2O_{Mn}H_2O)$	^{IV}Pb-DES	2.40	0.08	2.55	-	3.30	0.01	-35.16	5.92E+25	25.8	5.92E+30	5.92E+31	5.92E+32	5.92E+33
$Pb(2O_{Mn}H_2O)$-SES	$Pb(2O_{Mn}H_2O)$	^{III}Pb-SES	2.33	0.03	2.40	-	3.36	-	-38.30	1.19E+28	28.1	1.19E+28	1.19E+28	1.19E+28	1.19E+28
$Pb(2O_{Mn}2H_2O)$-SES	$Pb(2O_{Mn}2H_2O)$	^{IV}Pb-SES	2.35	0.03	2.55	0.01	3.38	-	-33.72	5.21E+24	24.7	5.21E+24	5.21E+24	5.21E+24	5.21E+24
$Pb(2O_{Mn}2H_2O)\cdot 2H_2O$-DCS	$Pb(2O_{Mn}2H_2O)\cdot 2H_2O$	^{IV}Pb-DCS	2.32	0.01	2.53	0.05	3.88	0.00	-33.20	2.17E+24	24.3	2.17E+24	2.17E+24	2.17E+24	2.17E+24
$Pb(3O_{2Mn}3H_2O)$-TCS	$Pb(3O_{2Mn}3H_2O)$	^{VI}Pb-TCS	2.23	0.02	2.55	0.03	3.59	0.11	1.84	-	-	-	-	-	-
$Pb(3O_{2Mn})\cdot 3H_2O$-TCS	$Pb(3O_{2Mn})\cdot 3H_2O$	^{III}Pb-TCS	2.29	0.03	-	-	3.72	0.06	-17.90	1.32E+13	13.1	1.32E+23	1.32E+25	1.32E+27	1.32E+29